accepted to AJ 20171204

Robo-AO Discovery and Basic Characterization of Wide Multiple Star Systems in the Pleiades, Praesepe, and NGC 2264 Clusters

Lynne A. Hillenbrand[1], Celia Zhang[1], Reed L. Riddle[2], Christoph Baranec[3], Carl Ziegler[4], Nicholas M. Law[4], John Stauffer[5]

ABSTRACT

We identify and roughly characterize 66 candidate binary star systems in the Pleiades, Praesepe, and NGC 2264 star clusters based on robotic adaptive optics imaging data obtained using Robo-AO at the Palomar 60" telescope. Only ∼10% of our imaged pairs were previously known. We detect companions at red optical wavelengths having physical separations ranging from a few tens to a few thousand AU. A 3-sigma contrast curve generated for each final image provides upper limits to the brightness ratios for any undetected putative companions. The observations are sensitive to companions with maximum contrast $\sim 6^m$ at larger separations. At smaller separations, the mean (best) raw contrast at $2''$ is 3.8^m (6^m), at $1''$ is 3.0^m (4.5^m), and at $0.5''$ is 1.9^m (3^m). PSF subtraction can recover close to the full contrast in to the closer separations. For detected candidate binary pairs, we report separations, position angles, and relative magnitudes. Theoretical isochrones appropriate to the Pleiades and Praesepe clusters are then used to determine the corresponding binary mass ratios, which range from 0.2-0.9 in $q = m_2/m_1$. For our sample of roughly solar-mass (FGK type) stars in NGC 2264 and sub-solar-mass (K and early M-type) primaries in the Pleiades and Praesepe, the overall binary frequency is measured at ∼15.5% ± 2%. However, this value should be considered a lower limit to the true binary fraction within the specified separation and mass ratio ranges in these clusters, given that complex and uncertain corrections for sensitivity and completeness have not been applied.

Subject headings: stars:binaries:visual, open clusters and associations

1. Introduction

More than half of all stars are found in multiple star systems. As reviewed by e.g. Goodwin et al. (2007), Duchene & Kraus (2013), and Reipurth et al. (2014), stellar multiplicity properties appear to be set within the first few million years of a star's life. Binary frequency is observed to increase with primary star mass, from <25% for stars near the hydrogen-burning limit to >90% for stars near the top of the initial mass function. The similar distributions in mass ratio and semi-major axis for both main sequence and pre-main

[1]Department of Astronomy, California Institute of Technology, Pasadena, CA 91125, USA; lah@astro.caltech.edu

[2]Caltech Optical Observatories, California Institute of Technology, Pasadena, CA 91125, USA

[3] Institute for Astronomy, University of Hawaií at Mañoa, Hilo, Hawaií 96720-2700, USA

[4]Division of Physics and Astronomy, University of North Carolina at Chapel Hill, Chapel Hill, NC 27599-3255, USA

[5]Spitzer Science Center, California Institute of Technology, Pasadena, CA 91125, USA

sequence binaries, suggests that the same formation processes occur over varying core masses, and that mild core fragmentation of collapsing gas clouds is the most appropriate theory for multiple-system formation (as reviewed by Boss, 1995; see also Offner et al. 2010).

In addition to having approximately the same distance from Earth, members of a star cluster form at the same time, from the same gas cloud, and have similar age and chemical composition. Thus, studying members of young clusters provides insight into star formation and evolution. A "top-down" theory describing the formation of stars in clusters invokes cloud compression and fragmentation through shocks due to supersonic turbulence. Approximately Jeans-mass fragments then collapse into single or, under further fragmentation, into binary and higher order multiple star systems that may then undergo further subsequent dynamical evolution, including binary disruption and/or capture, as reviewed by e.g. Goodwin & Kroupa (2005) and Bodenheimer (2011). The "bottom-up" theory (e.g. Shu et al. 1987) describes turbulence shocked gas that collapses directly into cores which become opaque to the radiation generated from conversion of gravitational energy, and continue to accrete gas. These objects evolve from near the $\sim 10^{-3}$ $M_{\odot}$ opacity-limited fragmentation limit, all the way up to become stars. In this model, binaries at $\lesssim$100 AU can form at later times through disk fragmentation, if the disk is cool enough.

Binary star characteristics such as multiplicity frequency, separation distribution, and mass ratio distribution can support or refute different elements of the various star and multiple star formation theories, with trends in these distributions as a function of primary star mass particularly important to quantify. Here, we examine wide-separation multiplicity in the Pleiades, Praesepe, and NGC 2264 clusters. We discuss the clusters in order of increasing distance because our observations are limited by both angular resolution (limiting detection of companions at constant photometric sensitivity), and by sensitivity (limiting the measurement of flux ratios at constant spatial resolution). Both resolution and sensitivity improve for closer targets.

The Pleiades cluster is one of the youngest and closest populous star clusters. It is well-studied and has had its constituent stars cataloged extensively (Rebull et al. 2016). The cluster has ∼1500 known members that are readily identified due to a significant common proper motion compared to background stars. From lithium depletion boundary methods, the cluster age was determined to be 125 ± 8 Myr (Stauffer et al. 1998b) while the mean distance is 136 ± 1 pc (Melis et al. 2014) and the mean extinction is often quoted as $A_V = 0.15$ mag. Praesepe also has been extensively cataloged (Rebull et al. 2017), aided by its distinct proper motion (e.g. Adams et al., 2002; Wang et al. 2014). The ∼ 1000 members of Praesepe are intermediate in age at 757±36 Myr and have a mean distance of 179±2 pc (Gaspar et al. 2009) and negligible reddening. NGC 2264 is a young ∼3 Myr cluster that is significantly further away, having a mean distance somewhere between ∼740 pc (Kamezaki et al 2014) and ∼913 pc (Baxter et al. 2009) with a range of extinction among the around 1500 known members. The cluster is a popular target for young star studies because it has moderately low extinction along the line of sight, and is next to a molecular cloud complex that reduces contamination from background stars.

As for exoplanet populations work, stellar multiplicity studies are conducted using techniques that sample different portions of the mass ratio $q = m_2/m_1$ versus semi-major axis, a, parameter space. Spectroscopic monitoring can detect radial velocity variations from either just one or both stars. Photometric monitoring searches for eclipses. Both methods sample close-in orbits, or small values of a, more readily than larger values of a. Direct imaging, the method employed here, samples only larger a values. All detection methods are most sensitive to binaries having small differences in mass / size / brightness, and become less sensitive towards lower mass, smaller, and fainter companions. Previous multiplicity work on the particular clusters we have investigated includes: radial velocity, eclipse, and direct imaging studies, as well as photometric identification of binaries.

Among both Pleiades and Praesepe cluster members, the binary fraction is found to be higher for the more concentrated members (Raboud & Mermilliod; 1998, 1999), which is attributed to the general trend of increased multiplicity towards higher mass stars that are more centrally concentrated than lower mass stars, perhaps due to the effect that their multiplicity increases the system mass and hence shortens the time scale for mass segregation (van Leeuwen, 1983).

In the Pleiades, Bettis (1975), Jaschek (1976), Stauffer et al. (1984), Pinfield et al. (2003), and Lodieu et al. (2012) assessed multiplicity based on photometric binary candidates, collectively covering A through L spectral types. Pinfield et al. (2003) concluded that the binary fraction increases towards lower masses while Lodieu et al. (2012) found a brown dwarf binary frequency using this technique of about 24% within 100 AU. These results have significant tension (at the factor of 2-3 level) with the direct imaging results covering the same mass and separation ranges that are discussed below. Previous and new radial velocity measurements of BAFG stars were used by Mermilliod et al. (1992, 1997) and Raboud & Mermilliod (1998) to characterize multiplity, resulting in a ∼25% spectroscopic binary fraction, consistent with the field star population. Adaptive optics direct imaging of G and K dwarfs was used by Bouvier et al. (1997) to estimate a binary fraction of 28±4% between 11 and 910 AU, consistent with the field star population. Martin et al. (2000), Bouy et al. (2006), and Garcia et al. (2015) all searched using HST for binaries among small samples of brown dwarfs, finding results consistent with the low binary fraction of ∼15% or less in the field for the mass and separation range. Notably, the majority of their newly resolved systems had been identified previously as photometric binary candidates (Raboud & Mermilliod; 1998). Richichi et al. (2012) identified several Pleiades binaries from lunar occulation observations.

In Praesepe, Bettis (1975), Jaschek (1976), and Pinfield et al. (2003) identified photometric binary candidates in this cluster as well. Bolte (1991) confirmed the early candidates as true binaries via spectroscopy. Later, Boudreault et al. (2012) and Khalaj & Baumgardt (2014) addressed multiplicity in a statistical sense with the latter authors measuring a multiple fraction of 8.5±1.6% and then claiming a true binary+triple fraction of 35%. Radial velocity measurements were used by Mermilliod & Mayor (1999) to measure spectroscopic binary orbits for FGK stars. A direct imaging search for multiplicity was conducted by Bouvier et al (2001) who estimate among G and K stars a binary fraction of 25±5% between 15 and 600 AU, in agreement with the field. Patience et al. (2002) surveyed B through M stars and found a smaller binary fraction over the same separation range, but also had a smaller sample. Peterson et al. (1984, 1989) identified several new Praesepe binaries from lunar occulation observations.

In NGC 2264, there have been few dedicated binary studies. Recently, Gillen (2015, 2017) has conducted a successful search for eclipsing systems and Kounkel et al. (2016) has identified spectroscopic binaries.

The overall conclusion from the above, and other papers on binarity in clusters, is that the dense cluster binary statistics are similar to the field star population binary statistics. This is in contrast to the results for young loose associations, which appear to have higher binary fractions, and lends support to the idea that the majority of the field star population formed in clusters rather than looser associations. An alternate hypothesis is that some binaries in young associations breakup during their pre-main sequence evolution.

2. Sample Selection for Binary Search

The input samples for our adaptive optics direct imaging companion search were selected as described below. A primary consideration was the availability of high cadence and high precision photometric datasets (either available at the time, or pending) for likely members of each cluster. All potential targets were

within the brightness range J≈10-13.5^m, selected as such via 2MASS photometry. From the input samples, the robotic scheduler for Robo-AO (Riddle et al. 2014) chose the actual targets of observation, as described below.

In NGC 2264, we included the 100 brightest classical T Tauri stars and the 100 brightest weak-line T Tauri stars having time series data from CoRoT. The CoRoT sample selection and results are described in e.g. Affer et al. (2013), Cody et al. (2014), Sousa et al. (2016), Lanza et al. (2016), Venuti et al. (2017), and Guarcello et al. (2017).

For the Pleiades and Praesepe clusters, the stars come from the $K2$ open clusters investigation of J. Stauffer (program IDs GO4032 and GO5032) which aimed to completely survey the bona fide members of these two clusters with high-precision, high-cadence optical photometry. The $K2$ time series sample selection and resulting data are described in detail in Rebull et al. (2016) for the Pleiades, and Rebull et al. (2017) for Praesepe. Pleiades stars were selected from the samples provided in Stauffer et al. (2007) and Bouy et al. (2015). Praesepe stars were compiled from the work of Jones & Cudworth (1983), Jones & Stauffer (1991), Klein-Wassink (1927), and Kraus & Hillenbrand (2007).

We obtained Robo-AO data for a total of 120 NGC 2264 members, 212 Pleiades members, and 108 Praesepe members. Knowledge regarding stellar multiplicity or lack thereof can inform the CoRoT and K2 lightcurve analysis.

3. Robo-AO

3.1. Hardware and Operation

Robo-AO (Baranec et al. 2014) was mounted on the Palomar 60-inch (1.5m) telescope before being moved in 2015 to the Kitt Peak 2.1m telescope (Salama et al. 2016; Jensen-Clem et al. 2017). At Palomar, the instrument was capable of imaging more than 200 objects per night.

Robo-AO is the first autonomous laser AO system (Baranec et al. 2014). It uses a 10-W ultraviolet laser for a guide star, which releases a 35-nanosecond laser pulse every 100 microseconds, and records the Rayleigh-scattered, returning photons to determine the correction (Riddle et al. 2015). The laser pulse is focused at 10 km. Wavefront aberrations are sampled at 1.2kHz which is sufficient to measure and correct the wavefront errors of the Palomar 1.5m telescope. The 44″ field-of-view of the Robo-AO visible camera is contained within the well-corrected diffraction-limited image area.

Besides the laser-launch system, the instrument consists of: a set of support electronics; a Cassegrain instrument package that houses a high speed electro-optical shutter, wavefront sensor, wavefront corrector, science instrument and calibration sources; and a single computer that controls the entire system. A master sequencer to control hardware subsystems creates an efficient overall observing system.

A queue scheduling program selects Robo-AO targets, optimizing the desired science targets among the practical constraints. A robot sequencer points the telescope and configures the associated system. A laser acquisition process involves a search algorithm to move the uplink steering mirror; the entire instrument configuration takes less than 30 seconds after telescope slew. During observations, telemetry is used to maintain focus and detect drops in laser return to continually adapt to conditions. Data are stored and processed in a computer system separate from the instrument control (Baranec et al. 2014). An Andor iXon DU-888 EMCCD images the science field at 8.6Hz (116 msec per individual frame) with the images saved

in data cubes for later processing.

The Robo-AO system can be used to build a sizable sample of moderate-contrast diffraction-limited images of stars within just a few nights.

3.2. Data Acquisition and Image Processing

Images of 446 targets in our three clusters were collected using the Robo-AO system on 2014, November 7-11, and 2015, March 3. Either an SDSS i' filter or an LP600 long pass filter with a 600 nm cut-on was used, the latter for sources fainter than R $\approx 13^m$ given the increased filter breadth but similar effective wavelength.

The observing sequence for a single target, described in detail in Baranec et al. (2014), begins with a queue scheduling program that optimizes among scientific priority, slew time, telescope limits, prior observing attempts, and laser-satellite avoidance windows. The science camera, laser, and adaptive optics system are configured as the telescope slews. Once pointed at the new target, the laser is acquired with a search algorithm moving a steering mirror, the adaptive optics system is started, and an observation is performed with no adaptive optics correction to estimate seeing conditions. Once the laser is acquired, the adaptive optics correction is started, removing residual atmospheric wavefront aberrations at 100Hz using a 12 x 12 actuator deformable mirror.

Total exposure times were either 120 sec or 300 sec, depending on source brightness. The raw data files consist of multiple data cubes of visible camera frames generated at 8.6Hz. When a cube reaches a size of 1GB (about 256 frames) it is closed and a new cube generated. In a 120 (300) sec exposure, about 1032 (2580) individual frames are generated.

The Robo-AO image processing pipeline is described in detail in Law et al. (2014ab). Each of our images was dark-subtracted, flat-fielded, and tip-tilt-corrected. Tip-tilt image motion was corrected using an object brighter than $\sim 16^m$ in the science image field, with a post-facto shift-and-add routine in the pipeline; in the case of our observations, the tip-tilt star was the main target. The images from each data cube were then stacked into a composite image with an up-sampled plate scale of 21.55 mas/pixel[1]. The data pipeline can select only a percentage of the best quality frames for inclusion in the final image (as is done with so-called "lucky imaging"), but in practice all Robo-AO frames are used in producing the final output science image.

Image cutouts of 400×400 pixel^2 (about $8.6''$ by $8.6''$), centered on each target star, were made for the subsequent analysis steps. Then a locally optimized PSF was created for each target from at least 20 sources observed nearby in time and airmass to the target. The reference PSF images were other science images taken temporally close to the science observation (within 1-2 hours); any drift in the PSF during a night should be slow. The target PSF is modelled using a linear combination of the reference PSFs (employing the LOCI algorithm; Lafreniere et al. 2007). If a reference PSF does not correlate with the target PSF, the algorithm does not include it in the model.

This empirical PSF was subtracted from the target stacked image cutout, and both it and the remainder image were saved along with the cutout. Figure 1 illustrates a PSF-subtraction sequence.

[1]This is half the pixel scale quoted in Riddle et al. (2015) since the images in the present data set are oversampled by a factor of two.

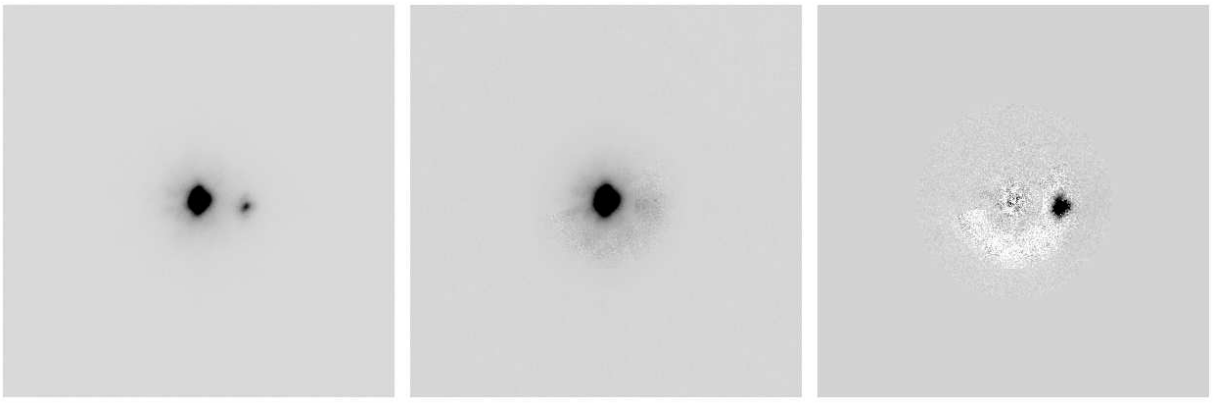

Fig. 1.— For AK IV-314, a binary system, shown are the stacked image cutout (left), the PSF image assembled from images surrounding the leftmost image in time (center), and the PSF-subtracted remainder image (right) that isolates the secondary star.

We note that in some images, artifacts from the data acquisition and processing produced apparent "triple systems" that are identifiable because of their linear alignment on the image. Software was used to remove this effect, but it failed for some targets ($< 1\%$ of the sample) and they had to be discarded from further analysis.

Each good final image stack contains either only a single source, or a detected candidate binary pair. For most of the targets, the stacked image cutout allowed us to identify, measure separations and position angles, and photometer the binary components. However, in cases where the secondary star is at high enough contrast or intrinsically too faint to be detected in the initial cutout, the PSF-subtracted image can be used to determine multiplicity and measure the properties of the secondary.

3.3. Image Quality Analysis

Image quality was used to assess the performance of the AO system and to determine the significance of the point sources detected in an observation.

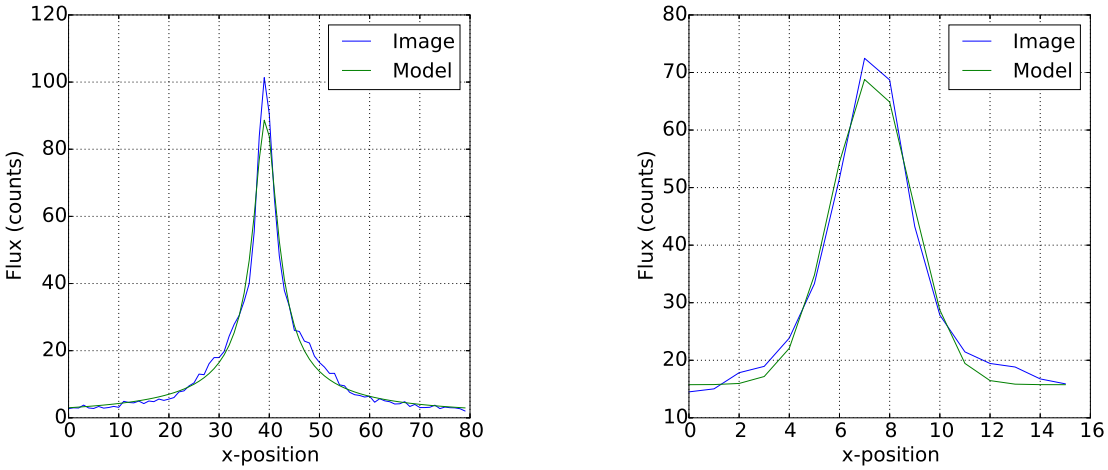

Fig. 2.— Example PSF models, evaluated at whole pixel values, and matched to cuts across Robo-AO image data. Left: 2D Moffat model of source BPL 167. Since the peak of the model is not located at the center of a pixel, and partial pixel values are interpolated in the plot, the peak is not well-represented graphically but is better estimated numerically. This model matches the image wings, but slightly overestimates the FWHM in the image core. Right: 2D Gaussian model of source CSIMon-0722. Relative to the Moffat model, the Gaussian model better matches the FWHM in the image core, but is worse in the image wings.

We modeled the primary point-spread function (PSF) on each image to assess image quality and to monitor its variation across the data set. High-quality images have smaller FWHMs and are produced

when the AO correction delivers a diffraction-limited PSF. Larger FWHM images occur when the PSF is dominated by uncorrected atmospheric turbulence, or poor seeing. Due to the image registration process, in cases of exceptionally poor correction, a single bright central pixel results from the stacking of seeing limited images (see discussion in Law et al. 2014). To find the FWHM of each stacked cutout image, we fit curves with different functional forms to the flux profile; examples are shown in Figure 2.

We first fit two-dimensional Moffat functions, of the form

$$f(x,y) = A(1 + \frac{(x-x_o)^2 + (y-y_o)^2}{\gamma^2})^{-\alpha}$$

where x_o and y_o describe the centroid position, x and y are the spatial coordinates on the image, and A, γ, and α are free parameters. Following the profile fit, its FWHM was defined as

$$FWHM = 2\gamma(2^{1/\alpha} - 1)^{0.5}.$$

In any given image, the number of pixels at essentially the background sky level far exceeds the number of pixels with significant amounts of flux, so we restricted the fitting box size around the primary. However, the Moffat fit failed to produce sensible results if the wings of the PSF were not entirely captured. We thus began with a 10×10 pixel ($0.22'' \times 0.22''$) box and incremented the box side length in 5 pixel steps, until a minimum FWHM was found. Based on visual examination, the Moffat fits tended to overestimate the FWHM. For some very faint sources, however, the FWHM was underestimated since the error term used to constrain the Moffat fit did not interpolate between pixels, greatly exaggerating the image peak.

We next fit two-dimensional Gaussian functions, of the form

$$g(x,y) = Ae^{-\frac{(x-x_o)^2+(y-y_o)^2}{2\sigma^2}} + C$$

with free parameters A, C, σ. The FWHM is then

$$FWHM = 2(2log(2))^{0.5}\sigma.$$

As for the Moffat fitting, the box size for the Gaussian fit was restricted. An additional challenge for the Gaussian fitting was that too few points could be considered when fitting the model. We thus began with a fitting box of length four times the Moffat-derived FWHM, and decremented it 1 pixel at a time until the RMS of the residual error of the centroid coordinate and its eight neighbors was below 0.1; we limited the box size to a minimum of 10×10 pixels.

Figure 3 illustrates the relationship between FWHM and source brightness derived under each model; Moffat fits are systematically larger than Gaussian fits. Figure 3 also illustrates the FWHM distribution in arcsec and demonstrates that the images are, for the most part, diffraction limited. The vast majority of estimated FWHMs are 3-10 pixels, or 0.07-0.22$''$ with a minority in a tail extending to outliers as high as 50 pixels, or 1.1$''$, which implies negligible AO corection for these several objects. However, given that the diffraction limit of the Palomar 60-inch telescope at Robo-AO wavelengths is $\lambda/D = 0.25 \times 0.75\mu m/1.52m = 0.12''$, or $\sim$5.5 pixels, FWHM values less than this (formally $1.028 \times \lambda/D$) are spurious; these are attributed to the image stacking process, which for low signal-to-noise sources can enhance a central peak noise spike. The underestimated FWHM values are not important for the photometry, which used a diffraction-limited aperture. The rise in FWHM with source brightness is expected, as the size of the PSF would increase. However, there is also a group of dimmer stars with unexpectedly large FWHMs, which we attribute to the AO correction not working as well due to the faintness of the stars, poor seeing, or possibly telescope motions – all of which can spread out the PSF of fainter objects.

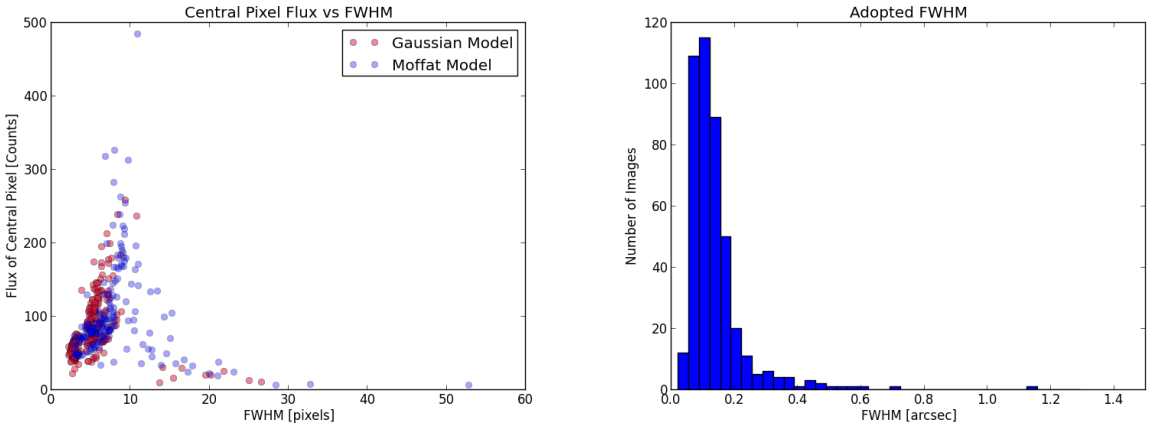

Fig. 3.— FWHM relation to source brightness, for both the Gaussian and the Moffat functional fits (left panel), and final adopted FWHM value as given in Table 1 (right panel).

The shape of the PSF varies as observing conditions and equipment performance change. It is for this reason that we combine local-in-time images in creating the empirical PSFs for subtraction from individual sources (Figure 1). Consequently, the theoretical model that most effectively approximates the PSF also changes over time. For each final image set, we therefore chose whichever model (Moffat or Gaussian) produced a smaller central-9-pixel RMS residual error term, in order to define the FWHM. The mean and median FWHM values are 6.45 and 5.51 pixels or 0.14 and 0.12″. For the high FWHM, faint sources, the Moffat fit yields better results. Similarly, for the low FWHM, bright sources, the Moffat fit also yields better results.

The FWHM values are reported in Table 1 and, as expected, are anti-correlated with the contrast sensitivity limits that are presented below.

4. Analysis of Detected Binaries

To determine the existence of binarity, we first used the DS9 V7.3.2 software[2] to examine the final image of each target. Overall brightness and contrast was varied, and contour plots were produced in identifying the candidate binaries.

4.1. Astrometry

DS9 was also used to roughly gauge the relative locations of the constituent stars in a pair. For improved precision, we used the Aperture Photometry Tool (APT; Laher, 2015) software[3] to determine the pixel centroids of each star in the initial cutout images. APT operates via a GUI with which users may

[2]http://ds9.si.edu/

[3]http://www.aperturephotometry.org/

manually place an aperture on a source. APT then uses iterative methods to compute centroid positions and, as discussed in the next section, aperture fluxes (Laher et al. 2012).

Before we could calculate the binary separations and position angles, we had to correct each primary centroid for image distortion (Riddle et al., 2015). Each cutout image has a reference coordinate with respect to the earlier stage full image taken by the Robo-AO instrument, enabling us to apply the published distortion correction. We then calculated the separation and rotation for each binary using the corrected centroids and knowledge of array orientation relative to true north. Finally, pixel separations were converted to physical separations in AU adopting the plate scale sampling of 21.55 mas and respective distances of 136, 175, and 740 pc for the Pleiades, Praesepe, and NGC 2264 clusters.

An appropriate typical error for the measured separations is $\sim 0.02''$, and for the measured position angles is ∼0.1-0.3 deg; the true error in the latter is dominated by an additional uncertainty in the instrument orientation, perhaps up to 1.5 degree based on repeated calibrations using globular cluster fields (Baranec et al, 2016).

4.2. Photometry

By convention, the star that is visibly brighter is designated as the primary, and its companion is the secondary. To obtain the difference in brightness between the two stars of each binary system, we used APT to measure the magnitude of each source inside an aperture, along with an uncertainty. Aperture corrections are not needed, since we are measuring relative magnitudes and the PSFs of each star are the same, given that they appear in the same image.

We used Model F for background correction within APT, which is a non-annulus based local estimate for the sky background considering a grid size of 64 pixels and window size of 129 pixels. The other five sky subtraction models APT offers take the mean, median, or mode of a manually placed sky-annulus, set the sky value manually, or apply no sky subtraction. We decided against using any of the models that are based on a sky annulus since the target stars are very large with respect to the image size, and of varying size and FWHM, so determining sky annulus radii introduced an unnecessarily arbitrary element to the analysis. For very faint secondary stars or binary systems with small separations, the algorithm used by APT to obtain centroids could not pinpoint the secondaries on the initial cutouts. In these cases, we used the PSF-subtracted remainder images to measure position centroids and magnitudes.

We explored for each image both a constant aperture of radius of 5 pixels ($0.11''$, containing about 83% of the encircled energy), and a custom aperture of radius 10-30 pixels, sufficient to cover 92-96% of the flux, even for the poor-quality images, for each member of each binary. The magnitude difference discrepancies between the constant aperture and the custom aperture form a roughly gaussian distribution. Our final photometry values come from the smaller aperture, in order to avoid contamination from the other member in the pair. Figure 4 illustrates the APT-reported measurement error as a function of the APT-reported instrumental magnitude.

For all detected binary systems, we computed magnitude differences and associated errors. We performed an independent check of the photometry using the pipeline described in Law et al. (2014) and Ziegler et al. (2017). For sources with close separations, the later values are preferred given the explicit de-blending, reducing the measured contrast for these objects over straight aperture photometry. Excluding these outliers, the mean contrast difference between the two methods was 0.01 mag and the dispersion 0.14

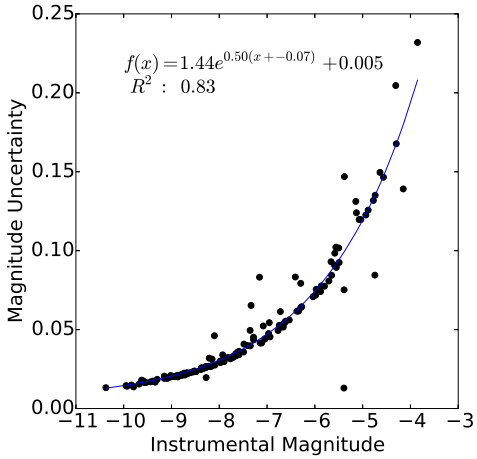

Fig. 4.— Photometric measurement error as a function of source brightness for the APT photometry. As expected, the uncertainties increase exponentially towards fainter magnitudes. The legend provides the fit results and corresponding coefficient of determination, which ranges between 0-1 where 1 would indicate a perfect fit within the expected variance. High outliers represent images with higher than typical noise. Low outliers occur in cases where secondary stars were found using the PSF-subtracted image. An approximate zero point scaling is that -8 mag on the instrumental scale corresponds to roughly 12.75 mag on a Vega scale. The photometry thus spans the magnitude range ∼10.5-16.5 mag.

mag, with point-to-point agreement at the <1-2 sigma level.

A significance for each companion detection was calculated using the methods employed in Ziegler et al. (2017). Briefly, the local noise as a function of separation from the target star is measured by sliding a 10-pixel diameter aperture within concentric annuli centered on the target star. The signal within the aperture at each position is measured, and the mean and standard deviation of the set of signals in each annulus is calculated. If the annulus contains an astrophysical source, the measured signals for that annulus are sigma clipped to remove the outlier signals associated with the source. An aperture is subsequently placed on the observed nearby star, and the signal compared to the local noise to estimate the detection significance.

Table 2 reports contrast values and a significance for each companion detection, both measured as described above.

5. Analysis of Images with No Detected Companions: Contrast Limits

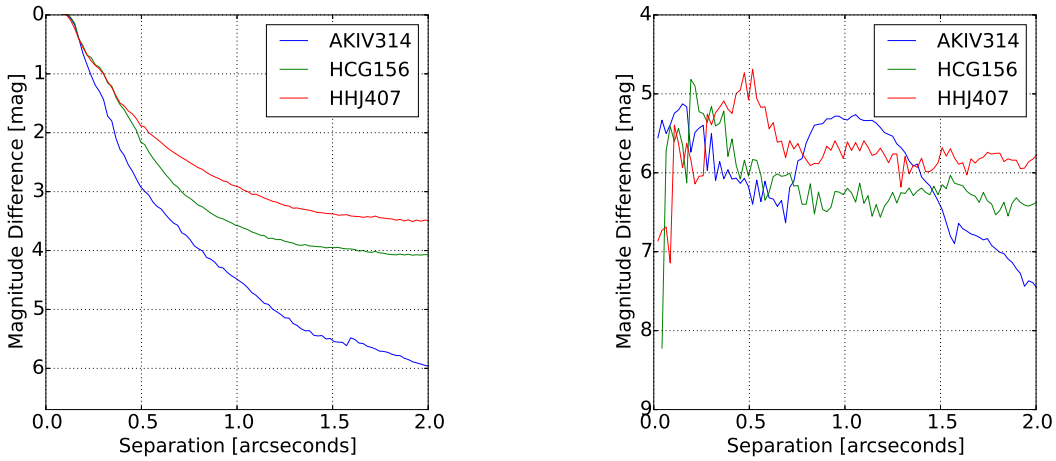

Fig. 5.— Contrast curves for three stars of varying image quality; raw contrast is on the left and PSF-subtracted contrast on the right. The stars illustrated are: AK IV-314, which was one of the most well-imaged stars, but is a binary system with separation of 1.03″; the secondary has been subtracted before generating the contrast curves (resulting in the artifact discontinuity around 1.6″). HCG-156 is representative of the mean performance, and is a single star. HHJ-407 is about one standard deviation away from the mean performance. As illustrated in the right panel, PSF subtraction improves the contrast by several magnitudes, though below ∼0.2″ (roughly $2 \times \lambda/D$), companion detection is still not possible. The broad bump for AK IV-314 is the residual of the seeing halo of the subtracted companion.

Only a fraction of the observed sources had identifiable companions. To assess our ability to detect binary stars and determine upper limits for undetected companions, we generated contrast curves for each final image. A contrast curve denotes the separation-dependent relative brightness level a secondary star needs to exceed for detection in the image. Naturally, at decreasing separations from the primary, secondary stars need to be increasingly brighter in order to be detected. An experimental contrast curve was generated by isolating the PSF of the primary and background-subtracting, then finding the median counts within a sky annulus encompassing 38 to 43 pixels from each centroid position. The PSF was then scaled down and placed into the original image at a series of random separation and random primary-secondary magnitude differences. The modified image was examined visually to see if the inserted secondary stars could be detected by eye, leading to rough contrast estimates of 3-6^m at 0.5-3″.

A more sophisticated algorithm for theoretical contrast curve generation involved first converting all

pixels into polar coordinates with origin at the primary star centroid. Next, around a circle describing the polar points at a given separation, we placed the maximum number of 5-pixel-radius tangent circles (apertures). For separations less than 7 pixels, a set number of three such apertures were used, placed 120 degrees apart. For each of the 5-pixel-radius apertures around each circle, the enclosed flux was measured, with the fluxes of partial pixels estimated using the ratio of areas within and outside the 5-pixel-radius aperture. Then, the standard deviation and the mean of all the fluxes measured at a given separation was found. The $3-\sigma$ contrast limit was generated at each separation using $3\times$ the standard deviation added to the mean flux level at that separation. Stated as a formula, we computed the contrast at separation r as

$$C(r) = -2.5 \times log(SNR_{threshold} \times \sigma(S_r) + mean(S_r))$$

where S_r is the set of flux values within an annulus around r, and $SNR_{threshold} = 3$. For binary stars, the procedure was modified to exclude those 5-pixel radius apertures with centers located within 30-pixels of the secondary star center.

Contrast curves were generated for every final image. Figure 5 illustrates the results for three examples of varying image quality. In Table 1, we provide the contrast values as magnitude differences at 0.5, 1, 2, and 3″ angular separation, for all sources. The tabulated contrast curve data exhibit approximately normal distributions, with means and standard deviations at the four separations of: 1.92 ± 0.46 at 0.5″, 3.01 ± 0.63 at 1″, 3.83 ± 0.84 at 2″, and $3.97^m \pm 0.91^m$ at 3″.

In order to further investigate the data quality, we examined the relationship between measured image FWHM and the change in the contrast values between 1″ and 0.5″. The correlation affirms that steep contrast curves come from low FWHM, high quality data. Anomalously poor contrast curves have large FWHMs and are generally due to fainter sources and poor image quality.

As a check on multiplicity, the contrast curves themselves were examined for bumps that could indicate binary stars. One new binary, of no particular dimness, that was overlooked in the earlier binary idenfication analysis was found in this manner: CSIMon-0021.

6. Cluster Multiplicity Results

Our Robo-AO survey covered about 10% of the known cluster membership in each cluster (ranging from 8% of known NGC 2264 members to 14% of known Pleiades members). The NGC 2264 sample is comprised largely of FGK spectral types, while the Praesepe and Pleiades samples are largely K and early M types.

Figure 6 illustrates the color-magnitude diagrams for known members of the three clusters, with those detected as singles or binaries in Robo-AO data highlighted. Figure 7 shows for a broader sample of Pleiades and Praesepe members, a color-magnitude plane in which the binaries stand out from the main cluster sequences somewhat better. The morphology of the Pleiades and Praesepe plots is consistent with the roughly main-sequence nature of these clusters, while the NGC 2264 plot is both pre-main sequence and dominated by color excesses due to extinction and dust disks. The main point is that the distributions of both the Robo-AO observed stars, and the detected binaries, are consistent with the general distribution of similar-color and magnitude objects.

We present a total of 66 candidate wide separation binaries - 32, 8, and 26 in the Pleiades, Praesepe, and NGC 2264, respectively (see Table 2). Relative to the number of binaries indicated in Table 1, there are fewer sources listed in Table 2 since some members of pairs were found twice: as companions to each

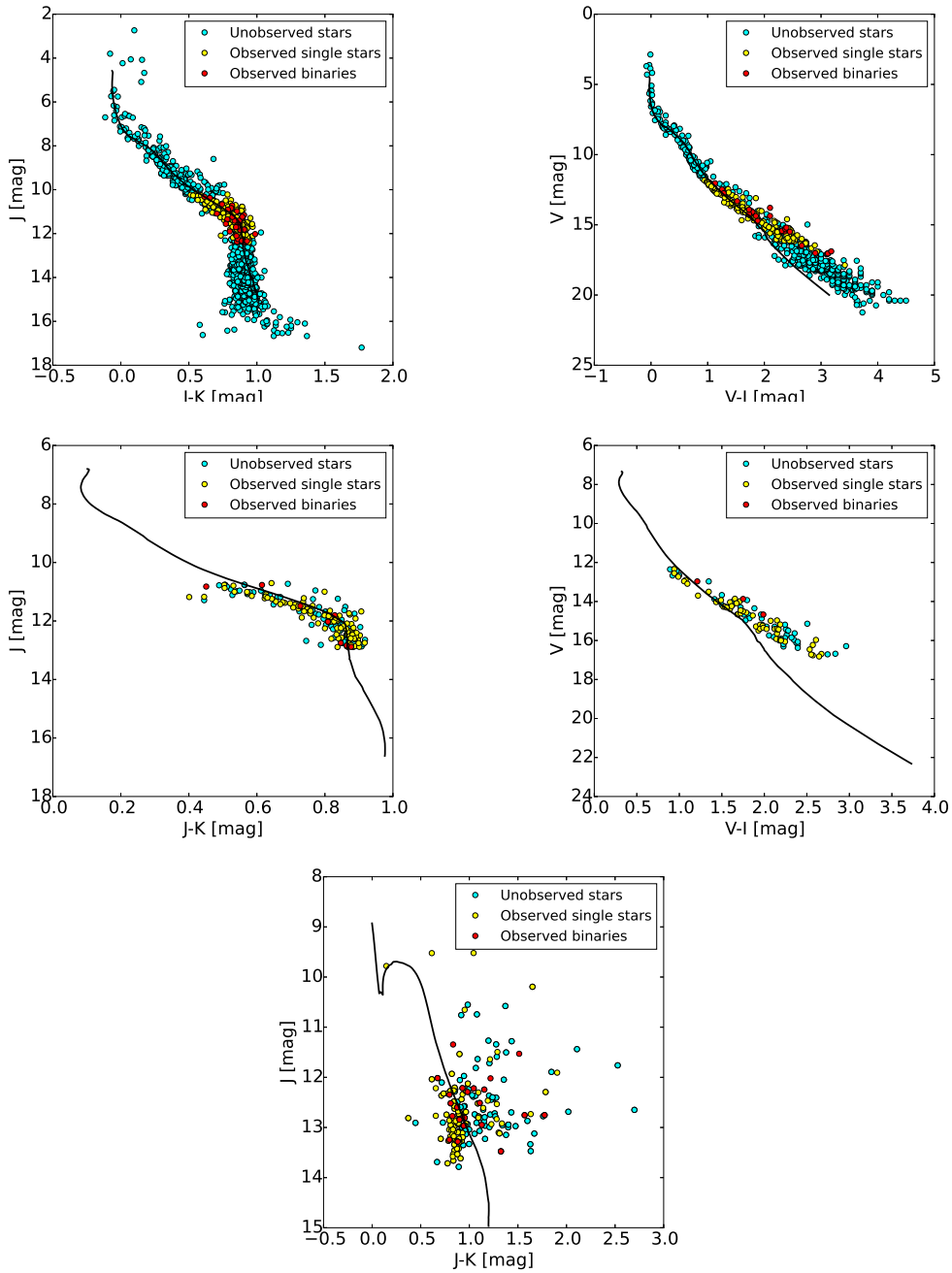

Fig. 6.— Color-magnitude diagrams using 2MASS (Cutri et al. 2003) near-infrared and literature optical photometry for the Pleiades (top), Praesepe (center), and NGC 2264 (bottom). In each panel, shown are: unobserved cluster members for which K2 time series photometry exists (cyan), Robo-AO observed single stars (yellow), Robo-AO detected pairs (red), and a theoretical isochrone at the appropriate age, distance, and average reddening for the cluster. The Robo-AO observed samples typically span about two magnitudes in brightness within each cluster; for the Pleiades, the full color-magnitude sequence is shown, for context, while for Praesepe and NGC 2264 just the magnitude range of relevance to Robo-AO is shown. Clear cluster loci can be seen for Praesepe and the Pleiades, but for NGC 2264 the locus is smeared due to the combined effects of circumstellar disks and extinction.

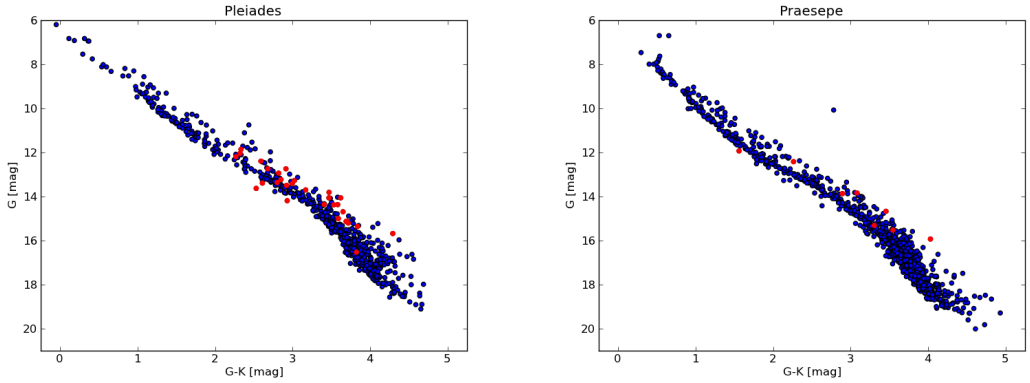

Fig. 7.— Location of the identified binaries (red) in an optical-infrared color-magnitude diagram, based on Gaia G-band (van Leeuwen et al. 2017) and 2MASS K-band (Cutri et al. 2003) photometry of the entire clusters. Relative to the main Pleiades and Praesepe cluster sequences, identified binary pairs stand out somewhere better in this color-magintude diagram than in the infrared-only color-magnitude diagram of Figure 6.

other when imaged separately. Among the binaries, just 5, 2, and 0 in the three respective clusters were revealed in a literature search as having their companions previously known. These confirmations (10% of our reported binary sample) provide confidence in our methods and detections overall, and further, allow the consideration of color information since the previously identified binaries had been observed at infrared wavelengths. We expect the separations to be about the same given the large cluster distances, but our reported magnitude differences will be larger in the optical than in the infrared, due to the expected redder color of the fainter companions, relative to their primaries.

Figure 8 presents the image gallery of our Robo-AO detected binary systems. There were 78 images containing candidate binaries, with 70 unique sources excluding repeats and poor quality images. Figure 9 illustrates the magnitude differences as a function of pair separation. Sources detected at higher contrast than the nominal limits come from better-than-average quality images or from the PSF-subtracted images; we note that this subset of high contrast companions is located within ∼1-1.5″, suggesting that they are true bound companions. The median pair separation is 1.1″ with the peak between ∼0.5-1.0″ and continued decline towards a flat distribution beyond ∼2″. Beyond 4″, the data become incomplete in position angle due to the square images. In physical units, the right panel of Figure 9 illustrates the rough segregation of companion sensitivity by distance. As NGC 2264 is further away, we were not sensitive to separations below ∼200-500 AU. Meanwhile, we detected binaries in the 30-500 AU range in the Pleiades and Praesepe samples, and to higher contrast levels than in NGC 2264.

Notably, there are many images on which binaries are detected at magnitude differences exceeding the individual “raw” contrast values listed in Table 1, and/or are more than three standard deviations better than the nominal contrast at a given separation (left panel of Figure 5). These high contrast outliers are due to the use of PSF-subtracted images, which were generated for all final images. The PSF-subtracted data naturally have significantly better contrast, down to below 5 mag for most targets, as illustrated in the right panel for the three examples shown in Figure 5. Five binary systems have brightness ratios of more than four magnitudes. Two of these, including the most significant outlier at the smallest separations, could not be seen in the initial image cutouts, but are clearly present in the PSF-subtracted images (and were detected

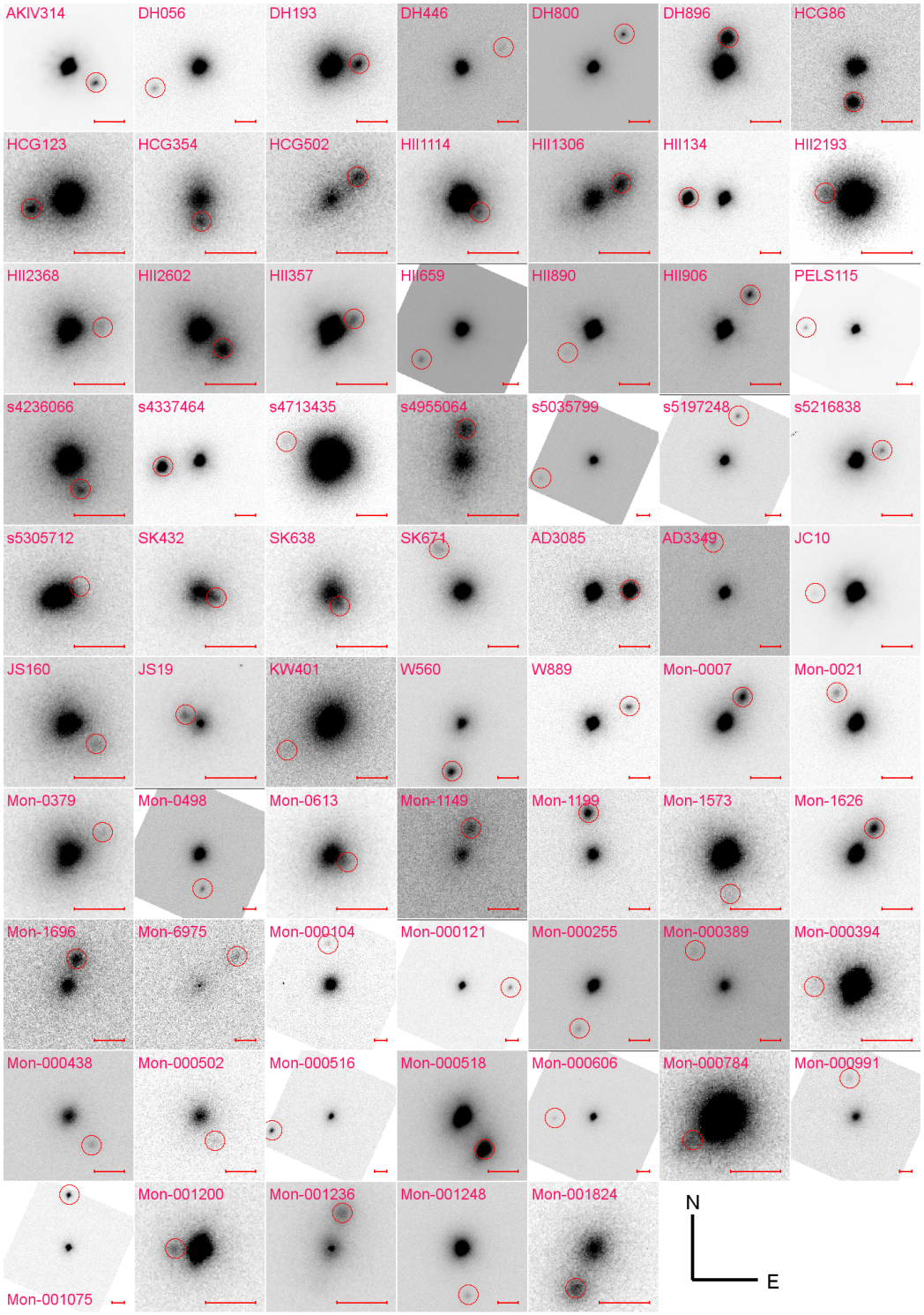

Fig. 8.— Robo-AO images of detected binaries; north is up and east is *to the right*. Red circles indicate the secondaries and red bars indicate a constant angular size of 1″. There are five different spatial scales, depending on the pair separation. Images are individually scaled in depth so as to highlight the binaries. Labels correspond to lines in Table 2, which provides the separations, position angles, differential magnitudes in the red optical, and detection significance for each system.

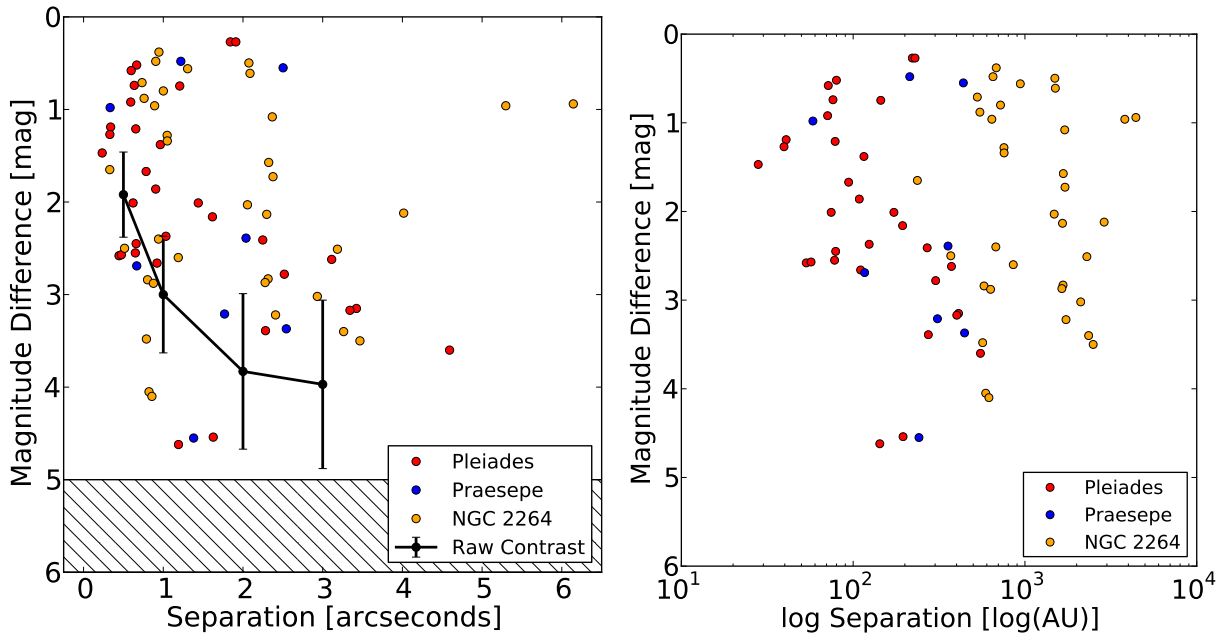

Fig. 9.— Separation vs. difference in magnitude for detected binary systems. Members of the three clusters are individually color-coded. Left panel is in empirical units, and includes the mean 3σ raw contrast curve, and standard deviation among the contrast curves for the entire data set; PSF subtraction enables sensitivity down to 5-6 mag of contrast for most targets, as shown in Figure 5. Right panel is in physical units of AU; apparent is the reduced sensitivity to small-separation companions for NGC 2264, due to the larger distance of this cluster, as well as the lack of sensitivity for Pleaides beyond ∼585-820 AU and Praesepe beyond ∼750-1050 AU, due to the maximum search radius imposed by image size. There is no correlation between separation and magnitude difference, in either panel.

in that manner). The other high brightness ratio systems were identified in the non-PSF-subtracted data in observations with exceptionally good contrast curves.

Results for the individual clusters are presented below. The raw multiplicity fraction across the three clusters, counting a total of 70 visual binary systems among 441 distinctly imaged targets with good Robo-AO imaging, is thus 15.9% ± 1.9% (or 15.1% ± 1.9% if duplicate pairings where each component was observed as the primary are removed). This fraction is comparable to the fraction of multiples found by Baranec et al. (2016) and Ziegler et al. (2017) using the same equipment but targetting a much older field star sample of comparably bright sources. However, the binary fraction varies significantly among the clusters with NGC 2264 (where we are sensitive to mainly wider separations and smaller magnitude differences, in a younger cluster) ∼50% higher, Pleiades at about the mean value, and Praesepe ∼50% lower. Because of the different cluster distances and ages, as well as the varying observing conditions during data acquisition, the sensitivity to companion separation and mass varies. Furthermore, the targets have different primary masses in NGC 2264 relative to the Pleiades and Praesepe samples, since the observations were constrained within the same apparent brightness ratio. For these reasons, the necessary but complex and uncertain incompleteness corrections required to turn our raw multiplicity fractions into fractions for specific a and $q = m_2/m_1$ ranges, given the primary star m_1 ranges, have not been applied.

6.1. The Pleiades at 136 pc

In the Pleiades cluster, 34 binary systems (including 2 pairs that were observed twice and identified as binaries of each other, making 32 unique pairs) were found among 212 targets.

HII 1306, a 0.60″ separation and Δm_{opt}=0.58^m system was also identified as a binary by Richichi et al. (2012), who reported separation 0.65″ and Δm_K=0.33^m. HII 134, a 1.84″ separation and Δm_{opt}=0.27^m system was also identified as a binary by Bouvier et al. (1997), who reported separation 1.83″ and Δm_K=0.13^m. Bouvier et al. (1997) also found HII 2193 which we identify as a separation 0.66″ and Δm_{opt}=2.45^m system; the previously reported separation is 0.69″ and Δm_K=1.71^m. Finally, for HII 357 we report a companion with separation 0.47″ and Δm_{opt}= 2.57^m while Bouvier et al. (1997) found separation 0.50″ and Δm_K=1.64^m.

For HII 890 we report a companion at separation 1.19″ and Δm=4.62^m while Bouvier et al. (1997) found separation 1.74″ and Δm_K=5.41^m, declaring the secondary source a background field object. This is the only detected pair with apparent relative motion between the components, and it is also the only pair with a bluer color for the secondary relative to its primary.

A raw multiplicity of 16.0% ± 1.4% was obtained from our observations of Pleiades KM primaries.

Notes on individual sources: One of the final images, HII 370, contained a false tripling artifact of the image acquisition, and thus could not be analyzed. One of the single stars, s4798986, was also excluded from analysis due to poor imaging. Three likely single stars, BPL 273, HII 34, and HCG 194, were "lumpy" rather than cleanly detected as binaries. Uncertainties regarding these targets add to the uncertainty of our reported multiplicity fraction.

6.2. Praesepe at 175 pc

Out of the 108 Praesepe targets, 8 were observed to be likely binaries.

As for the Pleiades, several of our optically identified Praesepe systems appear in previous literature announcing detected companions. KW 401 is reported as a 1.77″ separation and Δm_{opt}=3.21^m system while Bouvier et al (2001) detected KW 401 as a triple system with one component at 1.69″ and Δm_K=2.30^m at a similar position angle as our detection, and another component at separation 1.78″ and Δm_K=5.4^m that we do not see, presumably due to large optical-infrared color. We also detected W 560 as a 2.50″ separation Δm_{opt}=0.55^m system which Bouvier et al (2001) report with separation 2.43″ and Δm_K=0.92^m.

The observed multiplicity frequency for our Praesepe sample of KM primaries, is 10.2% ± 1.9%.

Notes on individual sources: One of the binary systems, JS 494, was excluded from analysis due to an additional false tripling artifact of the image acquisition. JS 231, a likely single star, and KW 566, likely a binary system, both have poor image quality and also could not be properly analyzed. Uncertainties regarding these targets add to the uncertainty of our reported multiplicity fraction.

6.3. NGC 2264 at 740 pc

Among 120 NGC 2264 targets, 34 (including 8 pairs that were observed twice and identified as binaries of each other, making 26 unique pairs) likely binaries were detected. There is no previous dedicated study of visual binaries in this cluster; a few such sources are known within the separation range to which we are sensitive (e.g. S Mon at 27 AU, R Mon at 530AU, and AR6 at 2100 AU), but we did not observe any of these objects. The observed multiplicity for our NGC 2264 target group of FGK primaries, is 27.3% ± 4.1%.

Notes on individual sources: Images for likely binary systems CSIMon-0394, CSIMon-0890, and CSIMon-0894 were poor, and thus photometry could not be performed so the 3 targets were excluded in our analysis. CSIMon-0618 and CSIMon-0486 are most likely singles, but also are of poor quality. Uncertainties regarding these targets add to the uncertainty of our reported multiplicity fraction.

6.4. Mass Ratios

The mass ratio of each identified binary system was estimated using theoretical isochrones that relate magnitude to mass. The pre-main sequence and main sequence isochrones of Siess et al. (2000) were employed in conjunction with the NextGen+AMES atmospheres of Haushildt, Allard, & Baron, (1999) and Allard et al. (2000) to generate V, I_C, J, and K_s magnitudes. We interpolated isochrones at 125 Myr and A_V = 0.15 mag, assuming a DM=5.67 for the Pleiades, and at 757 Myr and A_V = 0.00 mag, assuming a DM=6.22 for Praesepe. Due to the significant and target-dependent extinction in NGC 2264, combined with the potential influence of circumstellar disks at J and K, the mass ratio exercise was not carried out for members of this star-forming region. Color-magnitude diagrams for the Pleiades and Praesepe clusters in J vs J-K_s, J vs J-H, and V vs V-I_C demonstrate that the chosen isochrone set is a reasonable match to the cluster sequences. Generally, calculated isochrones are too blue and/or too faint for lower mass stars, especially in V vs V-I_c, compared to open cluster data; the Siess et al. (2000) models are a closer match to empirical data than most. We adopt J vs J-K_s for the mass decomposition, due to both the isochrone match and the uniform availability of data from 2MASS for our sample stars.

Previously measured magnitudes of our targets consist of the combined brightness of both stars for our identified pairs. These composite magnitudes (Table 1) were decomposed using the flux ratios tabulated in Table 2. While the flux ratios are measured in the LP600 or the SDSS i' filters, and would roughly

correspond to previous measurements in the I_C-band, such I_C-band magnitudes are not readily available for most of the sample. Instead, the abundant J and K_s magnitudes from 2MASS were used. Furthermore, as illustrated in Figure 6, the near-infrared brightness and color predictions are better in the near-infrared than in the optical for low mass stars. For each cluster, the point on the age-appropriate J vs J-K_s isochrone closest to each binary system was found. Then the theoretical I_C magnitude corresponding to these J and K_s magnitudes was decomposed into the constituent magnitudes of the two stars. Once again using the isochrones, the corresponding mass to each magnitude was found, and a ratio was determined for primary star m_1 and secondary star m_2. As the isochrones did not include stars under 0.1 $M_\odot$, for some of the faintest secondaries only an upper limit for the mass ratio was obtained.

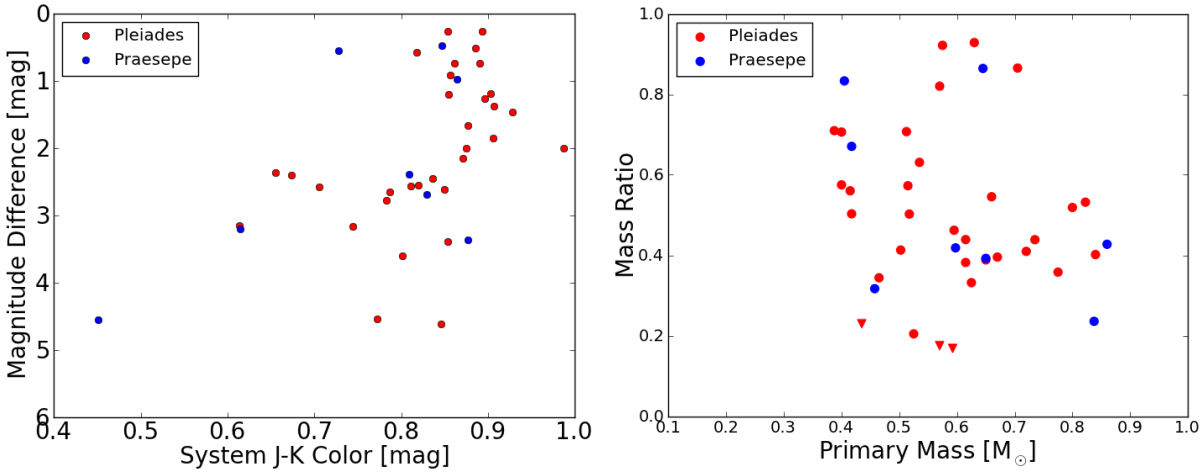

Fig. 10.— Magnitude difference as a function of system composite color (left) and corresponding inferred mass ratio as a function of primary mass (right) for the Pleiades (red, with upper limits indicated by inverted triangles set by the lowest masses available from the adopted evolutionary tracks) and Praesepe (blue) binary samples. As the distributions are dominated by small number statistics, no conclusions can be drawn beyond illustration of the range in q of the detected binaries.

Figure 10 illustrates the mass ratios as a function of primary mass. The Robo-AO data set spans a range in $q = m_2/m_1 \approx 0.2 - 0.9$ (see Table 2). Small number statistics, and the lack of incompleteness corrections, prevent us from drawing any conclusions regarding the true mass ratio distribution at the wide separations probed by the data set (Figure 9).

7. Discussion and Summary

Our optical multiplicity survey of 120 members of NGC 2264, 212 Pleiades members, and 108 Praesepe members covered in each case approximately 10% of the cluster membership cataloged to date. In NGC 2264, ours is the first high spatial resolution survey. In the Pleiades and Praesepe, previous similar work (notably by Bouvier et al. 1997 in the Pleiades, and by Bouvier et al. 2001 and Patience et al. 2002 in Praesepe) has been conducted at infrared wavelengths, though in sum covering a comparable number of stars to our study.

We identified 66 unique binary systems, only 7 of which were previously known. Given the small contrast

ratios and close separations, the majority of the newly identified companions are likely to be physically bound. Towards the low-contrast widest pairs, and the highest contrast close pairs, boundedness becomes less likely. We can assess the likelihood of chance superposition of faint foreground or background objects using a simulation of galactic stellar populations. We queried the TRILEGAL (Girardi et al., 2005, Girardi et al. 2012) V1.6 model[4] over 1 deg^2 fields towards each of the clusters, so as to establish a representative sampling of the contamination on few arcsec scales. The raw star counts brighter than $i = 17$ mag (see Figure 4) were scaled down to the 8.6″ by 8.6″ field-of-view of RoboAO to arrive at an expected 0.0025, 0.0181, 0.0087 contaminating stars per observation towards the Pleiades, Praesepe, and NGC 2264 clusters, respectively. Multiplying by the number of sources observed in each cluster, results in 0.5, 2.0, and 1.0 expected interlopers that we could be incorrectly calling binaries. However, these numbers are upper limits if one considers the smaller separations actually occupied by the observed companion distribution (see left panel Figure 9). Specifically, we would expect only 0.08, 0.33, and 0.17 total contaminants from the three clusters at $< 3.5''$ – where nearly all of the observed companions are located – and that any such contaminants would be close to the magnitude limit and therefore at the higher contrast levels. Future work involving proper motions and colors is required in order to definitively establish binarity versus field star contamination.

Our observations were sensitive to only those companions located beyond the peak of the separation distribution produced by Duquennoy & Mayor (1991) and Raghavan et al. (2010) for solar neighborhood field stars. Our observations also targetted only a narrow magnitude range, which corresponds to different primary mass ranges and secondary mass sensitivities at the different cluster distances. Thus, we can not make meaningful comparisons to the features of the field star distributions in either separation or mass ratio.

Nevertheless, the results of our work broadly sample mass ratios $q = m_2/m_1 = 0.2 - 0.9$ around primary stars with $\sim 0.4 - 0.9 M_{\odot}$. The measured parameters for individual objects will be valuable for future studies aimed at placing the multiplicity results for single-age clusters in the context of field star samples which have diverse ages, though better characterized multiplicity properties. Additional high spatial resolution survey work that would complete our multiplicity census for these important clusters should be carried out.

We acknowledge the Caltech SURF (Summer Undergraduate Research Fellowship) program for partially supporting the work of C. Zhang. Russ Laher provided appreciated guidance on use of the APT. Luisa Rebull provided the catalog photometry used in creating Figure 7. We thank Emma Hovanec for literature research on the targets of this study. The Robo-AO system at Palomar was supported by the collaborating partner institutions, the California Institute of Technology and the Inter-University Centre for Astronomy and Astrophysics, and by the National Science Foundation under grants AST-0906060 and AST-0960343, by the Mount Cuba Astronomical Foundation, and by a gift from Samuel Oschin. C.B. acknowledges a Sloan Fellowship. We remain grateful to the Palomar Observatory staff for their efforts in support of astronomical research, and to the Palomar Observatory Director for the allocation of observing time to this project.

8. References

Adams, J. D., Stauffer, J. R., Skrutskie, M. F., et al. 2002, AJ, 124, 1570

Affer, L., Micela, G., Favata, F., Flaccomio, E., & Bouvier, J. 2013, MNRAS, 430, 1433

[4]http://stev.oapd.inaf.it/cgi-bin/trilegal

Allard, F., Hauschildt, P. H., & Schweitzer, A. 2000, ApJ, 539, 366

Baranec, C., Riddle, R., Law, N. M., et al. 2014, ApJ, 790, L8

Baranec, C., Ziegler, C., Law, N. M., et al. 2016, AJ, 152, 18

Baxter, E. J., Covey, K. R., Muench, A. A., et al. 2009, AJ, 138, 963

Bettis 1975, PASP 87, 797

Bodenheimer, P. H. 2011, Principles of Star Formation: , Astronomy and Astrophysics Library. Springer-Verlag Berlin Heidelberg, 2011 (Chapter 6).

Bolte, M. 1991, ApJ, 376, 514

Boss, A. P. 1995, Revista Mexicana de Astronomia y Astrofisica Conference Series, 1, 165

Boudreault, S., Lodieu, N., Deacon, N. R., & Hambly, N. C. 2012, MNRAS, 426, 3419

Bouvier, J., Rigaut, F., Nadeau, D., 1997, Astronomy and Astrophysics, 323, 139.

Bouvier, J., Duchêne, G., Mermilliod, J.-C., & Simon, T. 2001, A&A, 375, 989

Bouy, H., Moraux, E., Bouvier, J., et al. 2006, ApJ, 637, 1056

Bouy, H., Bertin, E., Sarro, L. M., et al. 2015, A&A, 577, A148

Cody, A. M., Stauffer, J., Baglin, A., et al. 2014, AJ, 147, 82

Cutri, R. M., Skrutskie, M. F., van Dyk, S., et al. 2003, The IRSA 2MASS All-Sky Point Source Catalog, NASA/IPAC Infrared Science Archive.

Duchêne, G., & Kraus, A. 2013, ARA&A, 51, 269

Duquennoy, A., & Mayor, M. 1991, A&A, 248, 485

Garcia, E. V., Dupuy, T. J., Allers, K. N., Liu, M. C., & Deacon, N. R. 2015, ApJ, 804, 65

Gillen, E., 2015, Ph.D. Thesis, University of Oxford

Gillen, E., Hillenbrand, L.A., Daivd, T.J., Aigrain, S., Rebull, L., Stauffer, J., Cody, A.M., & Queloz, D., 2017, ApJ, in press. (https://arxiv.org/abs/1706.03084)

Girardi, L., Groenewegen, M. A. T., Hatziminaoglou, E., & da Costa, L. 2005, A&A, 436, 895

Girardi, L., Barbieri, M., Groenewegen, M. A. T., et al. 2012, Astrophysics and Space Science Proceedings, 26, 165

Goodwin, S.P., Kroupa, P., Goodman, A., Burkert, A., 2007, Protostars and Planets V, eds. B Reipurth , D. Jewitt & K. Keil (University of Arizona Press: Tuscon), p 133-147.

Guarcello, M. G., Flaccomio, E., Micela, G., Argiroffi, C., Sciortino, S., Venuti, L., Stauffer, J., Rebull, L., Cody, A. M., 2017, å, 602, 10

Hauschildt, P. H., Allard, F., & Baron, E. 1999, ApJ, 512, 377

Jaschek, C. 1976, A&A 50, 185

Jensen-Clem, R., Duev, D., Riddle, R., Salama, M., Baranec, C., Law, N., & Kulkarni, S., 2017, PASP,

submitted (https://arxiv.org/abs/1703.08867)

Jones, B., & Stauffer, J. 1991, AJ, 102, 1080

Jones, B., & Cudworth, K., 1983, AJ 88, 215

Kamezaki, T., Imura, K., Omodaka, T., et al. 2014, ApJS, 211, 18

Khalaj, P., & Baumgardt, H. 2013, MNRAS, 434, 3236

Klein-Wassink, W. 1927, Publ. Kapteyn Astron. Lab. Groningen 41

Kraus, A. & Hillenbrand, L., 2007, AJ, 134, 6.

Kounkel, M., Hartmann, L., Tobin, J. J., et al. 2016, ApJ, 821, 8

Lafreniere et al. 2007, ApJ, 660, 770

Laher, R. Aperture Photometry Tool. Computer software. Aperture Photometry Tool. Vers. 2.5.1. Spitzer Science Center, 2015. Web. 13 July 2015.

Laher, R. et al., Publications of the Astronomy Society of the Pacific, Vol. 124, No. 917 (July 2012), pp. 764-781

Lanza, A. F., Flaccomio, E., Messina, S., et al. 2016, A&A, 592, A140

Law, N. M., Baranec, C., & Riddle, R. L. 2014, Proc. SPIE, 9148, 91480A

Law, N. M., Morton, T., Baranec, C., et al. 2014, ApJ, 791, 35

van Leeuwen, F. 1983, Ph.D. Thesis,

van Leeuwen, F., Evans, D. W., De Angeli, F., et al. 2017, A&A, 599, A32

Lodieu, N., Deacon, N. R., & Hambly, N. C. 2012, MNRAS, 422, 1495

Martín, E. L., Brandner, W., Bouvier, J., et al. 2000, ApJ, 543, 299

Melis et al. 2014, Science 345, 1029

Mermilliod et al 1992, AA 265, 513

Mermilliod et al 1997, AA 320, 74.

Mermilliod & Mayor 1999, AA 352, 479

Offner, S. S. R., Kratter, K. M., Matzner, C. D., Krumholz, M. R., & Klein, R. I. 2010, ApJ, 725, 1485

Patience, J., Ghez, A. M., Reid, I. N., & Matthews, K. 2002, AJ, 123, 1570

Peterson, D. M., & White, N. M. 1984, AJ, 89, 824

Peterson, D. M., Baron, R., Dunham, E. W., et al. 1989, AJ, 98, 2156

Pinfield, D. J., Dobbie, P. D., Jameson, R. F., et al. 2003, MNRAS, 342, 1241

Raboud & Mermilliod 1998, AA 329, 101

Raghavan, D., McAlister, H. A., Henry, T. J., et al. 2010, ApJS, 190, 1

Rebull, L. M., Stauffer, J. R., Bouvier, J., Cody, A. M., Hillenbrand, L. A., Soderblom, D. R., Valenti,

J., Barrado, D., Bouy, H., Ciardi, D., et al. 2016, AJ, 152, 113

Rebull, L. M., Stauffer, J. R., L.A. Hillenbrand, A.M. Cody, J. Bouvier, D.R. Soderblom, M. Pinsonneault, 2017, ApJ, 839, 92

Reipurth, B., Clarke, C. J., Boss, A. P., et al. 2014, Protostars and Planets VI, 267

Richichi, A., Chen, W. P., Cusano, F., et al. 2012, A&A, 541, A96

Riddle, R. L., Hogstrom, K., Papadopoulos, A., Baranec, C., & Law, N. M. 2014, Proc. SPIE, 9152, 91521E

Riddle, R. L., Tokovinin, A., Mason, B. D., et al. 2015, ApJ, 799, 4

Salama, M., Baranec, C., Jensen-Clem, R., et al. 2016, Proc. SPIE, 9909, 99091A (https://arxiv.org/pdf/1608.02985.pdf)

Sarro, L. M., Bouy, H., Berihuete, A., et al. 2014, A&A, 563, A45

Shu, F. H., Adams, F. C., & Lizano, S. 1987, ARA&A, 25, 23

Siess, L., Dufour, E., & Forestini, M. 2000, A&A, 358, 593

Sousa, A. P., Alencar, S. H. P., Bouvier, J., et al. 2016, A&A, 586, A47

Stauffer, J. R., Hartmann, L., Soderblom, D. R., & Burnham, N. 1984, ApJ, 280, 202

Stauffer, J. R., Hartmann, L. W., Fazio, G. G., et al. 2007, ApJS, 172, 663

Venuti, L., Bouvier, J., Cody, A. M., et al. 2017, A&A, 599, A23

Wang, P. F., Chen, W. P., Lin, C. C., et al. 2014, ApJ, 784, 57

Ziegler, C., Law, N. M., Morton, T., et al. 2017, AJ, 153, 66

Table 1. Characteristics of Observed Targets

Cluster	Target[1]	R.A.	Dec.	V	I	J	K	Robo-AO multiplicity	FWHM[2]	Robo-AO Contrast Distribution			
										0.5"	1"	2"	3"
		[degrees]		[mag]					[pix]	[Δmag]			
Pleiades	AKIV 314	58.53719	24.33364	12.48	11.23	10.38	9.72	detected binary	9.1	2.92	4.47	5.96	6.22
	BPL 167	57.03671	25.02939	16.19	13.65	12.20	11.25	single	6.5	2.05	3.03	3.58	3.62
	BPL 273	58.21706	25.17400	16.27	13.73	12.38	11.53	likely single	4.8	1.68	2.85	3.32	3.34
	DH 027	53.29373	22.52204	15.55	13.36	12.12	11.25	single	6.0	2.06	3.27	3.81	3.86
	DH 056	54.10133	22.62379	14.14	12.37	11.35	10.56	detected binary	6.5	1.84	2.99	3.77	3.90
	DH 065	54.21886	23.26258	13.66	12.25	11.38	10.63	single	7.3	2.18	3.33	4.23	4.36
	DH 146	55.14717	20.96581	15.99	13.59	12.19	11.30	single	16.9	1.67	2.85	3.61	3.69
	DH 156	55.21359	23.59843	12.79	11.57	10.74	10.08	single	6.1	1.81	2.99	4.32	4.64
	DH 166	55.30749	23.38495	14.05	12.41	11.45	10.63	single	5.2	1.83	2.89	3.67	3.79
	DH 193	55.47359	23.45797	14.00	12.23	11.16	10.25	detected binary	5.9	1.82	2.92	3.92	4.16
	DH 249	55.74896	22.42427	13.98	12.34	11.45	10.59	single	5.9	2.04	3.39	4.50	4.66
	DH 318	56.04961	19.30539	15.10	13.10	11.95	11.05	single	3.8	1.37	2.46	3.52	3.71
	DH 446	56.60487	21.43823	17.01	14.11	12.37	11.52	detected binary	3.0	1.68	2.74	3.19	3.25
	DH 550	57.03197	25.31534	13.94	12.31	11.17	10.34	single	8.1	2.39	3.47	4.43	4.57
	DH 554	57.04240	23.00114	14.55	12.84	11.81	11.00	single	3.1	1.50	2.67	3.50	3.62
	DH 568	57.08264	23.60333	16.12	13.75	12.39	11.47	single	4.2	1.72	2.75	3.36	3.44
	DH 668	57.60395	20.70505	14.69	12.87	11.81	10.94	single	3.0	1.66	2.75	3.53	3.65
	DH 679	57.66373	25.39377	12.45	11.09	10.22	9.43	single	10.6	2.74	4.23	5.76	6.06
	DH 749	58.07687	22.01489			12.29	11.39	single	4.6	1.77	2.90	3.67	3.74
	DH 767	58.18894	25.27986	13.78	12.22	11.25	10.52	single	6.7	2.66	3.98	4.95	5.05
	DH 792	58.42924	20.83351	14.78	12.86	11.63	10.76	single	3.5	1.53	2.81	3.62	3.71
	DH 795	58.49216	20.48045	15.38	13.14	11.83	10.92	single	5.1	1.65	2.73	3.66	3.79
	DH 800	58.57845	25.49529	12.88	11.44	10.48	9.81	detected binary	7.4	2.76	4.09	5.30	5.43
	DH 803	58.61852	24.32115	14.20	12.49	11.45	10.62	single	7.8	2.93	4.26	5.10	5.22
	DH 851	59.32017	24.00923	12.79	11.53	10.66	9.95	single	8.9	3.04	4.61	6.00	6.19
	DH 854	59.39414	22.92576	13.88	12.37	11.43	10.64	single	4.5	1.58	2.91	3.92	4.11
	DH 875	59.84540	22.57136	14.33	12.54	11.49	10.56	single	6.9	2.51	3.59	4.32	4.38
	DH 877	59.86470	23.12379	13.38	11.94	10.95	10.13	single	5.4	1.70	3.01	4.34	4.58
	DH 896	60.26719	20.37270	15.47	13.11	11.81	10.91	detected binary	12.5	2.53	3.32	3.98	4.13
	HCG 64	55.51219	23.93164	16.32	13.59	12.02	11.13	poor quality	...	...	...	...	...
	HCG 68	55.54549	24.08572	15.95	13.44	12.03	11.15	single	7.6	2.24	3.26	3.77	3.83
	HCG 71	55.58974	24.66465	14.48	12.66	11.58	10.72	single	2.7	1.19	2.00	2.81	2.94
	HCG 75	55.60953	22.89466	14.45	12.64	11.55	10.72	single	5.5	2.19	3.42	4.33	4.44
	HCG 75	55.60953	22.89466	14.45	12.64	11.55	10.72	single	5.1	2.15	3.27	4.07	4.17
	HCG 77	55.62257	22.79060	15.16	13.07	11.80	10.92	single	6.0	1.99	3.37	4.33	4.44
	HCG 80	55.66761	23.98937	15.75	13.39	12.02	11.14	single	5.8	2.09	3.62	4.16	4.24
	HCG 86	55.67666	23.33937	17.04	13.92	12.25	11.39	detected binary	3.5	1.87	2.92	3.08	3.27
	HCG 93	55.73557	24.08277	16.24	13.54	12.08	11.23	single	5.0	1.98	2.96	3.48	3.51
	HCG 100	55.79060	24.69249	16.37	13.73	12.29	11.42	single	2.9	1.72	2.53	3.05	3.15
	HCG 101	55.76746	22.80098	15.16	12.96	11.68	10.79	single	4.7	2.02	3.16	3.75	3.81
	HCG 103	55.80444	24.65540	15.99	13.61	12.23	11.29	single	5.3	1.96	2.84	3.39	3.43
	HCG 123	55.92555	24.57316	15.43	13.12	11.83	10.96	detected binary	5.9	1.82	2.74	3.47	3.61
	HCG 141	56.03667	23.07990	15.43	13.21	12.00	11.11	single	6.3	2.21	3.55	4.34	4.41
	HCG 149	56.10337	24.76839	15.42	13.23	11.92	11.01	single	6.0	2.13	3.23	3.97	4.07
	HCG 156	56.11198	24.40883	16.07	13.58	12.39	11.45	single	5.4	2.16	3.57	4.07	4.09
	HCG 164	56.15741	22.92103	15.75	13.38	11.90	11.04	single	5.0	1.90	3.10	3.93	4.03
	HCG 181	56.31935	24.57570	16.18	13.70	12.32	11.43	single	5.2	1.99	3.48	4.00	4.04
	HCG 194	56.40298	24.65188	16.73	13.88	12.26	11.35	likely single	5.6	2.06	3.42	3.84	3.85
	HCG 214	56.52185	22.98165	14.00	12.32	11.33	10.50	single	5.3	1.72	3.01	4.05	4.23
	HCG 219	56.60576	24.16010	15.83	13.37	12.02	11.14	single	5.4	2.10	3.32	4.03	4.11
	HCG 244	56.72335	24.28751	16.24	13.57	12.06	11.21	single	4.6	1.96	3.06	3.68	3.73
	HCG 245	56.70325	23.06875	16.04	13.83	12.33	11.42	single	3.0	1.64	2.59	3.26	3.37
	HCG 247	56.73789	23.25067	15.50	13.29	12.01	11.13	single	4.6	1.61	2.69	3.57	3.73
	HCG 258	56.80691	23.83150	15.78	13.31	11.94	11.09	single	5.1	1.91	3.03	3.79	3.90
	HCG 263	56.85745	25.14251	16.91	13.98	12.36	11.45	single	4.4	2.10	2.92	3.30	3.35
	HCG 273	56.87747	24.37055	15.80	13.50	12.25	11.37	single	6.2	1.72	2.80	3.52	3.60
	HCG 277	56.88940	23.69250	15.74	13.16	11.76	10.93	single	4.7	1.78	2.94	3.78	3.91
	HCG 295	56.96228	24.50522	16.16	13.73	12.35	11.47	single	6.1	2.29	3.78	4.29	4.29
	HCG 317	57.10848	25.24475	15.46	13.25	11.96	11.09	single	5.9	2.05	3.16	3.95	4.07
	HCG 323	57.09437	22.87270	16.14	13.67	12.34	11.48	single	2.9	1.34	2.40	3.17	3.24
	HCG 324	57.12937	24.28148	16.01	13.57	12.25	11.34	single	23.2	0.97	2.16	2.82	2.89
	HCG 329	57.10627	22.21159	14.02	12.48	11.38	10.60	single	5.4	1.70	2.83	3.77	3.94
	HCG 332	57.11079	23.19161	17.45	14.12	12.19	11.36	single	3.0	1.79	2.67	3.06	3.14
	HCG 349	57.23895	24.32884	15.92	13.34	11.91	11.01	single	5.0	1.85	3.01	3.81	3.91
	HCG 353	57.25416	22.98044	15.39	13.23	12.03	11.15	single	4.6	1.67	2.76	3.61	3.75
	HCG 354	57.27441	23.73975	15.31	12.94	11.64	10.79	detected binary	3.1	1.39	2.44	3.22	3.31
	HCG 360	57.29681	22.17679	13.80	12.10	10.89	10.10	single	5.1	1.61	2.70	3.92	4.22
	HCG 362	57.31836	24.06367	15.52	13.03	11.69	10.75	single	5.1	1.81	3.02	3.88	4.01
	HCG 370	57.36514	24.53173	15.99	13.54	12.12	11.26	single	17.9	1.32	2.53	3.26	3.39
	HCG 376	57.39949	22.15148	13.98	12.07	10.87	10.02	single	5.0	1.60	2.82	4.05	4.29
	HCG 378	57.46580	21.30734	15.63	13.18	11.81	10.92	single	5.2	1.39	2.55	3.49	3.61
	HCG 398	57.59546	22.18836	14.51	12.64	11.46	10.59	single	3.0	1.30	2.32	3.31	3.49
	HCG 420	57.84946	22.11339	13.19	11.83	10.94	10.20	single	8.0	1.57	2.73	4.03	4.37
	HCG 423	57.81589	23.28227	14.84	12.87	11.70	10.82	single	2.9	1.53	2.51	3.30	3.40
	HCG 458	58.14359	22.50217	15.79	13.55	12.29	11.39	single	2.9	1.52	2.50	3.18	3.30
	HCG 460	58.20288	21.70787	14.76	12.77	11.57	10.66	single	3.3	1.66	2.73	3.58	3.65
	HCG 488	58.64497	21.88394	15.51	13.28	12.06	11.18	single	3.2	1.27	2.33	3.23	3.38

Table 1—Continued

Cluster	Target[1]	R.A.	Dec.	V	I	J	K	Robo-AO multiplicity	FWHM[2]	Robo-AO Contrast Distribution			
										0.5"	1"	2"	3"
		[degrees]			[mag]				[pix]	[Δmag]			
	HCG 489	58.61649	23.83542	13.07	11.48	10.47	9.66	single	5.3	1.47	2.68	4.11	4.52
	HCG 491	58.64004	25.67881	14.72	12.55	11.26	10.37	single	6.4	2.47	3.66	4.41	4.43
	HCG 495	58.71899	24.57624	13.17	11.59	10.64	9.83	single	8.3	3.07	4.56	5.97	6.11
	HCG 502	58.95302	23.92677	14.81	12.56	11.33	10.44	detected binary	3.2	1.43	2.47	3.23	3.31
	HCG 508	59.09788	24.83243	14.12	12.46	11.37	10.55	single	6.6	2.24	3.27	4.13	4.32
	HCG 511	59.23784	24.80964	16.04	13.51	12.16	11.23	single	6.1	2.23	3.10	3.64	3.72
	HHJ 407	54.89773	24.11842	15.67	13.39	12.07	11.18	single	4.8	1.88	2.90	3.49	3.56
	HHJ 418	54.59741	23.10811	15.25	13.11	11.90	11.04	single	5.0	1.74	2.71	3.49	3.61
	HHJ 439	59.40031	23.93124	14.78	12.85	11.69	10.77	single	7.9	2.84	4.09	4.77	4.82
	HII 1029	56.61927	24.75899	14.34	12.59	11.51	10.65	single	6.1	2.25	3.28	4.09	4.18
	HII 1039	56.61573	23.59269	12.96	11.52	10.59	9.82	single	7.3	2.17	3.50	4.94	5.24
	HII 1061	56.62991	24.11735	14.21	12.39	11.29	10.34	single	5.7	2.04	3.40	4.38	4.53
	HII 1081	56.63698	23.30532	14.61	12.72	11.64	10.78	single	3.2	1.62	2.72	3.47	3.53
	HII 1095	56.65739	24.74769	11.83	10.89	10.22	9.67	single	7.2	2.35	3.65	5.39	5.86
	HII 1103	56.64720	23.41173	14.77	12.85	11.69	10.72	single	3.8	1.84	2.91	3.60	3.72
	HII 1110	56.66201	24.52033	13.29	11.89	11.10	10.27	single	9.8	2.62	4.31	5.44	5.61
	HII 1114	56.66777	24.93103	14.10	12.30	11.09	10.38	detected binary	7.2	2.14	3.32	4.29	4.40
	HII 1124	56.66410	24.02968	12.32	11.24	10.45	9.86	single	8.3	2.22	3.60	5.21	5.62
	HII 1173	56.70505	24.60001	15.10	13.05	11.90	11.00	single	9.1	2.65	4.15	4.88	4.98
	HII 1220	56.72192	22.88094	11.74	20.74	10.23	9.72	single	7.9	1.69	2.97	4.71	5.36
	HII 1280	56.76493	24.15971	14.57	12.72	11.60	10.72	single	5.3	2.11	3.30	4.16	4.25
	HII 1286	56.76572	23.61632	15.35	12.89	11.56	10.60	single	3.0	1.75	2.70	3.35	3.44
	HII 1298	56.77825	23.71517	12.33	11.25	10.42	9.84	possible binary	6.5	1.78	3.16	4.79	5.08
	HII 1305	56.78060	23.22633	13.52	12.09	11.18	10.40	single	5.3	1.90	3.04	4.21	4.42
	HII 1306	56.78558	23.71081	13.51	22.51	10.72	9.90	detected binary	6.7	1.45	2.59	3.91	4.24
	HII 1321	56.78931	23.74218	15.22	12.85	11.55	10.66	single	3.2	1.74	2.82	3.58	3.69
	HII 133	55.90384	24.39394	14.26	12.53	11.48	10.64	single	7.1	2.34	3.47	4.30	4.36
	HII 1332	56.80637	23.71431	12.53	11.43	10.62	10.01	single	6.6	1.92	3.26	4.73	5.08
	HII 134	55.90260	24.23230	14.37	12.27	10.98	10.13	detected binary	5.5	2.46	3.49	3.99	4.20
	HII 1348	56.82526	24.39077	12.70	11.33	10.49	9.72	single	9.2	2.78	4.49	6.04	6.24
	HII 1454	56.89032	24.68422	12.86	11.62	10.81	10.13	single	10.7	2.43	4.20	5.53	5.70
	HII 146	55.90249	23.45393	14.52	12.71	11.58	10.73	single	5.2	2.20	3.42	4.31	4.41
	HII 1485	56.90865	24.89183	14.21	12.50	11.46	10.61	single	5.8	2.03	3.13	3.93	4.06
	HII 1512	56.90836	23.46805	13.51	12.10	11.08	10.33	single	5.2	1.73	3.08	4.26	4.44
	HII 1516	56.91822	24.30193	13.97	12.30	11.14	10.34	single	5.6	2.08	3.36	4.41	4.62
	HII 1531	56.92265	23.97194	13.58	12.11	11.07	10.31	single	7.3	2.39	3.57	4.58	4.75
	HII 1532	56.92158	23.74029	13.99	12.37	11.38	10.57	single	4.4	1.92	3.20	4.25	4.40
	HII 1653	56.99889	24.73134	13.50	12.00	10.95	10.16	single	8.2	2.46	3.65	4.79	4.98
	HII 1756	57.04577	23.50702	14.10	12.48	11.53	10.69	single	4.0	1.52	2.68	3.61	3.80
	HII 1785	57.07204	24.50442	14.29	23.29	11.51	10.69	single	6.4	1.91	3.16	4.41	4.66
	HII 1827	57.09486	23.97254	14.84	12.66	11.39	10.51	single	4.4	2.00	3.06	3.89	3.97
	HII 1883	57.11678	23.30077	12.66	11.43	10.52	9.84	single	6.3	1.73	3.09	4.65	5.01
	HII 189	55.95251	23.53937	13.96	12.33	11.39	10.56	single	7.4	2.45	3.56	4.34	4.44
	HII 191	55.96726	24.84159	14.50	12.66	11.51	10.65	single	7.0	2.40	3.53	4.22	4.32
	HII 2016	57.18931	23.33887	13.55	12.08	11.07	10.38	single	5.5	1.58	2.81	4.08	4.36
	HII 2034	57.20550	23.97732	12.65	11.50	10.66	9.99	single	6.6	1.81	3.16	4.70	5.02
	HII 212	55.98203	24.42639	14.30	12.55	11.51	10.65	single	6.4	2.10	3.19	4.03	4.08
	HII 2193	57.29698	23.55524	14.23	12.50	11.41	10.58	detected binary	4.9	1.76	2.84	3.72	3.89
	HII 2208	57.31408	24.56728	14.42	12.55	11.34	10.49	single	4.7	1.71	2.94	3.96	4.19
	HII 2209	57.30127	23.22835	14.48	12.66	11.53	10.72	single	3.3	1.40	2.52	3.53	3.69
	HII 2244	57.33579	24.77667	12.58	11.40	10.62	9.93	single	6.7	1.68	2.99	4.47	4.84
	HII 2368	57.39547	23.45468	14.35	12.48	11.24	10.42	detected binary	5.4	1.75	2.92	3.84	3.99
	HII 2407	57.42612	24.46306	12.19	11.17	10.36	9.78	single	8.2	1.88	3.30	4.98	5.39
	HII 2548	57.52108	24.12398	14.02	12.39	11.41	10.59	single	5.3	2.01	3.24	4.20	4.39
	HII 2602	57.55108	23.99589	15.49	13.04	11.70	10.85	detected binary	4.7	1.68	2.63	3.55	3.72
	HII 2870	57.71433	23.32910	12.51	11.40	10.63	10.02	single	6.9	1.97	3.26	4.81	5.22
	HII 2908	57.75963	25.05547	13.47	12.12	11.04	10.37	single	6.8	2.31	3.58	4.77	4.95
	HII 2966	57.80030	23.93263	14.86	12.90	11.77	10.90	single	3.3	1.74	2.83	3.62	3.71
	HII 2984	57.82023	23.82660	12.41	11.33	10.62	9.96	single	7.4	1.98	3.35	4.94	5.32
	HII 3104	57.90842	23.18317	13.47	11.85	10.85	10.03	single	5.1	1.62	2.80	4.09	4.43
	HII 3187	57.98889	23.33943	13.15	11.81	10.99	10.20	single	6.3	1.28	2.42	3.74	4.10
	HII 324	56.09127	24.76840	12.99	11.70	10.83	10.07	single	6.9	2.16	3.46	4.74	4.96
	HII 335	56.09609	24.06830	13.77	12.13	10.93	10.22	single	10.1	2.53	4.17	5.13	5.26
	HII 34	55.76223	24.66973	11.96	10.98	10.28	9.73	likely single	7.8	2.32	3.70	5.37	5.77
	HII 347	56.11372	24.84396	14.00	12.07	10.91	10.02	single	8.0	2.06	3.28	4.26	4.38
	HII 357	56.11670	24.17155	13.32	11.80	10.84	10.03	detected binary	10.5	2.42	4.08	5.26	5.42
	HII 370	56.13325	23.87521	14.44	12.38	11.28	10.45	poor quality	...	...	...	...	...
	HII 390	56.14754	24.00135	14.33	12.58	11.55	10.65	single	6.6	2.45	3.97	4.78	4.84
	HII 451	56.20904	24.91113	13.43	12.00	11.13	10.34	single	6.3	2.09	3.29	4.41	4.59
	HII 513	56.24568	23.38894	13.85	22.85	11.27	10.48	single	5.9	2.21	3.49	4.54	4.65
	HII 522	56.26360	23.83943	11.97	10.97	10.26	9.73	single	13.5	2.24	3.77	5.55	5.97
	HII 554	56.29993	24.58617	13.93	12.32	11.41	10.56	single	7.5	2.34	3.48	4.40	4.52
	HII 624	56.34788	24.85080	15.28	13.14	11.93	11.04	single	6.3	2.12	3.21	4.03	4.10
	HII 636	56.34248	23.47173	12.40	11.28	10.47	9.85	single	7.0	1.88	3.28	4.82	5.21
	HII 659	56.35824	23.43020	12.04	10.91	10.32	9.70	detected binary	7.5	1.98	3.41	4.99	5.42
	HII 673	56.37591	24.31265	15.74	13.35	12.05	11.13	single	8.9	2.38	3.87	4.60	4.68
	HII 686	56.38722	24.30324	13.52	12.02	11.06	10.22	single	9.2	2.68	4.19	5.24	5.42

Table 1—Continued

Cluster	Target[1]	R.A.	Dec.	V	I	J	K	Robo-AO multiplicity	FWHM[2]	Robo-AO Contrast Distribution			
										0.5"	1"	2"	3"
		[degrees]		[mag]					[pix]	[Δmag]			
	HII 740	56.42687	25.05709	13.40	12.11	11.27	10.50	single	8.4	2.51	3.75	4.80	4.93
	HII 762	56.43364	24.07410	14.23	12.51	11.51	10.64	single	6.2	2.42	3.87	4.68	4.77
	HII 813	56.47402	24.46912	15.23	12.81	11.46	10.57	single	5.7	2.54	3.76	4.42	4.48
	HII 879	56.52706	24.56741	12.79	11.59	10.79	10.11	single	7.3	2.21	3.69	5.19	5.40
	HII 882	56.51717	23.40553	12.95	11.62	10.54	9.84	single	6.7	1.93	3.28	4.81	5.19
	HII 883	56.52874	24.56280	13.05	11.75	10.91	10.29	single	9.5	2.66	4.28	5.63	5.86
	HII 890	56.53126	24.37438	14.71	12.83	11.71	10.86	detected binary	7.8	2.53	3.96	4.58	4.62
	HII 906	56.54122	24.67362	15.20	12.81	11.47	10.59	detected binary	7.4	2.44	3.79	4.26	4.41
	HII 915	56.53483	23.34752	13.79	12.26	11.26	10.40	single	5.5	1.94	3.09	4.16	4.39
	HII 930	56.55361	24.05437	14.20	12.48	11.43	10.60	single	6.4	2.26	3.35	4.16	4.28
	HII 974	56.58531	24.78548	13.96	12.34	11.34	10.54	single	7.9	2.22	3.45	4.45	4.55
	PELS 030	55.74674	22.90092	12.10	11.05	10.28	9.71	single	8.9	1.92	3.48	5.22	5.71
	PELS 066	56.89234	21.74684	12.33	11.22	10.53	9.90	single	8.3	2.19	3.54	5.19	5.55
	PELS 115	58.99328	24.54994	12.75	11.47	10.67	9.92	detected binary	9.3	2.95	4.55	6.02	6.27
	PELS 123	53.30793	23.00647	11.98	10.95	10.26	9.67	single	12.6	2.26	3.66	5.21	5.57
	PELS 162	59.38879	24.05319	12.11	11.09	10.45	9.86	single	8.5	2.49	3.71	5.38	5.79
	PELS 189	54.12626	24.01222	12.26	11.20	10.47	9.90	single	7.2	2.33	3.70	5.25	5.58
	PELS 192	58.87085	23.77245	14.12	12.46	11.42	10.59	single	5.1	1.59	2.73	3.74	3.96
	s4236066	61.72697	26.33548			12.02	11.04	detected binary	4.5	1.91	2.87	3.61	3.71
	s4337464	60.47535	23.05878			11.24	10.34	detected binary	5.8	2.40	3.14	3.48	3.81
	s4382488	57.42091	20.32433			10.70	9.85	single	5.2	1.54	2.84	4.16	4.46
	s4543478	58.35033	19.42136			12.17	11.29	single	3.9	1.76	2.71	3.29	3.39
	s4634206	62.50823	23.70343			10.77	9.88	single	7.9	2.30	3.54	4.49	4.62
	s4713435	55.66634	19.50882			11.56	10.78	detected binary	5.3	1.54	2.75	4.09	4.40
	s4728998	58.36222	19.40918			10.96	10.07	single	5.3	1.89	3.04	4.06	4.19
	s4745026	58.81555	19.62963			10.77	9.98	single	5.0	1.27	2.49	3.96	4.31
	s4798986	56.77226	20.44432			11.47	10.61	poor quality	...	...	...	...	...
	s4868524	58.91459	21.27280			11.82	10.90	single	4.7	1.42	2.49	3.47	3.66
	s4869367	59.01886	21.54522			12.06	11.16	single	5.1	1.71	2.80	3.47	3.53
	s4954485	57.76630	22.40479			11.61	10.73	single	4.8	1.53	2.61	3.76	4.02
	s4955064	58.03390	22.15069			12.33	11.44	detected binary	3.1	1.18	2.21	3.09	3.19
	s5003270	56.64497	22.93549			11.71	10.85	single	5.2	1.73	3.00	4.16	4.35
	s5021891	61.73343	22.03470			11.76	10.83	single	8.4	2.44	3.53	4.36	4.46
	s5035799	52.36702	22.66008			11.90	11.10	detected binary	10.7	2.16	3.41	4.26	4.40
	s5061696	59.19914	22.76893			11.57	10.72	single	6.5	1.74	3.14	4.43	4.69
	s5087225	61.75019	23.22893			11.82	10.91	single	6.3	2.14	3.29	4.16	4.28
	s5092529	61.15490	23.39764			12.09	11.36	single	5.6	2.40	3.32	3.85	3.92
	s5158273	57.07506	23.89151			11.81	10.96	single	14.3	1.84	3.05	4.13	4.32
	s5197223	60.36313	24.13064			11.21	10.42	single	7.5	2.51	3.72	4.69	4.81
	s5197248	60.24611	24.14241			12.11	11.26	detected binary	8.0	2.43	3.49	4.18	4.21
	s5216838	54.48581	25.01730			10.91	10.12	detected binary	7.6	2.54	3.67	4.65	4.75
	s5243866	61.50344	23.56855			11.41	10.57	single	7.3	2.33	3.45	4.21	4.26
	s5258893	62.51583	23.81220			11.81	10.92	single	8.9	2.48	3.65	4.50	4.61
	s5286016	57.84222	25.16613			11.49	10.66	single	4.9	1.88	2.91	3.70	3.83
	s5305712	59.55802	25.10770			12.34	11.41	detected binary	4.6	1.87	2.98	3.40	3.42
	s5339130	62.31372	25.09357			12.32	11.43	single	7.1	2.36	3.39	3.97	4.06
	s5446993	61.87268	25.58334			11.73	10.87	single	11.1	2.37	3.48	4.38	4.49
	SK 145	58.24641	24.90153	14.51	12.71	11.60	10.71	single	3.4	1.68	2.65	3.40	3.53
	SK 17	59.10409	23.09081	15.30	13.18	11.97	11.08	single	5.2	1.77	3.01	3.98	4.12
	SK 18	59.10803	24.28099	15.03	13.01	11.91	11.01	single	5.2	1.73	2.88	3.93	4.09
	SK 201	58.02321	22.58205	16.19	13.75	12.38	11.48	single	4.1	1.71	2.80	3.40	3.44
	SK 428	56.83680	25.08676	15.75	13.44	12.11	11.14	single	5.5	2.00	3.11	3.83	3.92
	SK 432	56.81370	25.11541	16.70	13.98	12.39	11.49	detected binary	3.4	2.00	2.72	3.03	3.19
	SK 638	55.86237	24.45272	16.89	13.71	12.32	11.42	detected binary	3.2	1.64	2.50	2.92	2.97
	SK 671	55.67456	24.19953	14.50	12.58	11.40	10.53	detected binary	3.5	1.77	2.68	3.44	3.59
	SK 687	55.57860	23.98952	14.69	13.07	12.05	11.17	single	9.0	2.29	3.54	4.40	4.49
	SK 724	55.41490	23.76308	14.58	12.77	11.69	10.87	single	3.0	1.73	2.77	3.49	3.58
	SK 773	55.13119	23.55067	15.24	13.13	11.95	11.06	single	5.7	2.09	3.08	3.68	3.77
Praesepe	AD 1166	127.20803	19.98898			12.34	11.46	single	6.2	2.44	3.43	3.98	4.04
	AD 1423	127.74003	20.66245			12.60	11.72	single	6.7	2.54	3.61	4.27	4.35
	AD 1427	127.74553	18.69473			12.46	11.59	single	2.5	1.04	1.70	2.46	2.62
	AD 1508	127.87447	20.41041			11.67	10.77	single	8.4	2.45	3.96	4.96	5.08
	AD 1512	127.88673	21.02444			11.89	11.12	single	8.7	2.52	3.82	4.92	5.07
	AD 1594	128.04449	21.34157			11.77	10.96	single	8.8	2.46	3.79	4.99	5.19
	AD 1660	128.18671	18.03616			12.64	11.75	single	25.0	1.09	1.88	2.35	2.37
	AD 2902	130.29385	19.93521			12.86	11.97	single	32.8	0.62	1.31	1.77	1.79
	AD 3085	130.60840	21.23086			12.75	11.90	detected binary	14.1	2.20	2.84	2.98	3.12
	AD 3128	130.69151	21.27121			11.73	10.92	single	8.0	2.75	4.02	4.96	5.07
	AD 3349	131.22446	21.61849			12.88	12.01	detected binary	9.5	2.33	3.20	3.50	3.53
	HSHJ 15	127.91855	19.79838			11.92	11.03	single	7.6	2.29	3.86	4.65	4.75
	HSHJ 393	130.45612	20.07673			12.84	11.97	single	2.3	1.15	1.62	1.97	2.01
	HSHJ 393	130.45612	20.07673			12.84	11.97	single	2.6	1.48	2.23	2.68	2.74
	HSHJ 510	132.31882	21.58671			12.41	11.53	single	4.5	2.09	2.65	2.87	2.78
	HSHJ 7	127.71260	19.35246			12.02	11.19	single	9.3	2.70	3.95	4.93	5.07
	JC 10	128.16444	19.95619			10.82	10.37	detected binary	9.4	2.38	4.36	5.56	5.88
	JC 85	129.26440	19.17812	13.63	22.63	11.44	10.73	single	5.0	1.56	2.86	4.15	4.37

Table 1—Continued

Cluster	Target[1]	R.A.	Dec.	V	I	J	K	Robo-AO multiplicity	FWHM[2]	Robo-AO Contrast Distribution			
										0.5"	1"	2"	3"
		[degrees]			[mag]				[pix]	[Δmag]			
	JS 107	129.01852	19.92030	14.65	12.96	12.00	11.16	single	3.5	1.79	2.84	3.56	3.65
	JS 109	129.02631	20.68332	15.65	13.50	12.32	11.45	single	6.0	2.23	3.47	4.19	4.29
	JS 113	129.04764	19.87787	15.49	13.56	12.53	11.66	single	5.2	1.72	2.80	3.50	3.58
	JS 117	129.06471	20.68605	15.41	13.29	12.51	11.63	single	6.0	2.26	3.48	4.17	4.25
	JS 118	129.06660	20.55313	14.57	12.78	12.04	11.23	single	5.5	2.37	3.61	4.25	4.30
	JS 12	128.13924	20.08009	13.29	22.29	11.28	10.63	single	7.2	2.28	3.77	4.98	5.15
	JS 128	129.10480	21.14903	16.06	13.82	12.88	11.98	single	5.7	2.30	3.26	3.71	3.74
	JS 131	129.11612	21.12115	14.04	12.44	11.72	10.96	single	7.0	2.67	4.02	4.83	4.87
	JS 132	129.11304	19.86518	15.44	13.28	12.10	11.23	single	5.1	1.77	3.18	4.10	4.19
	JS 14	128.20718	18.70174	13.04	22.04	10.71	10.06	single	6.9	1.56	2.91	4.45	4.85
	JS 140	129.15175	19.18522	14.48	12.75	12.02	11.20	single	3.2	1.66	2.85	3.68	3.77
	JS 145	129.17790	18.89524	14.27	12.75	11.59	10.84	single	6.1	1.77	2.87	3.87	4.03
	JS 15	128.21764	19.97664	13.07	22.07	11.15	10.56	single	11.0	2.59	4.04	5.30	5.46
	JS 152	129.21515	19.07641	14.01	12.33	11.58	10.86	single	3.5	1.62	2.61	3.70	3.92
	JS 155	129.22546	18.75687	12.73	21.73	11.00	10.47	single	6.1	1.61	2.73	4.14	4.53
	JS 156	129.24100	21.56546			11.95	11.12	single	7.9	2.69	3.95	4.98	5.17
	JS 159	129.23442	18.96334	14.97	12.82	11.78	10.91	single	3.0	1.59	2.48	3.18	3.35
	JS 160	129.23669	19.09112	14.67	12.68	11.80	10.97	detected binary	3.0	1.49	2.50	3.24	3.36
	JS 17	128.23193	18.73283			11.23	10.60	single	7.2	2.23	3.55	4.88	5.12
	JS 174	129.33295	19.05332	16.69	14.02	12.75	11.83	single	3.0	1.77	2.61	3.08	3.12
	JS 180	129.35999	19.13216	14.72	12.86	12.02	11.19	single	3.5	1.90	2.89	3.56	3.63
	JS 181	129.36856	20.60794	15.40	13.25	12.36	11.49	single	5.2	2.35	3.50	4.16	4.22
	JS 186	129.37938	19.10395	13.99	12.28	11.49	10.77	single	6.4	1.81	2.93	3.94	4.11
	JS 19	128.25166	20.71953			12.84	11.98	detected binary	3.6	2.19	2.76	3.20	3.23
	JS 21	128.26207	18.68265			11.33	10.68	single	5.4	1.80	3.09	4.42	4.64
	JS 227	129.59943	20.72803	14.50	12.78	12.08	11.30	single	7.4	2.76	3.89	4.43	4.47
	JS 23	128.28108	20.13007	13.86	12.21	11.68	10.93	single	6.2	2.30	3.76	4.59	4.69
	JS 231	129.61749	21.54611	13.31	22.31	11.00	10.20	likely single	9.5	2.71	4.15	5.31	5.47
	JS 242	129.65515	19.02114	13.74	22.74	11.35	10.61	single	4.9	1.90	2.97	4.04	4.24
	JS 246	129.68304	19.29398	16.76	14.19	12.83	11.96	single	2.4	1.33	1.99	2.40	2.45
	JS 256	129.73030	19.28382	15.92	13.78	12.63	11.74	single	2.6	1.26	2.00	2.64	2.77
	JS 264	129.76611	20.76324	15.96	13.77	12.57	11.72	single	7.9	2.67	3.72	4.24	4.29
	JS 302	129.90181	19.26051	14.38	12.78	11.81	11.01	single	3.3	1.54	2.53	3.40	3.59
	JS 317	129.94403	19.21780	15.28	13.38	12.35	11.51	single	5.1	1.84	2.92	3.72	3.83
	JS 318	129.96368	20.58054	16.23	13.66	12.49	11.59	single	5.5	2.17	3.55	4.06	4.08
	JS 344	130.04521	18.98251	16.72	14.17	12.87	12.01	single	2.7	1.74	2.45	2.78	2.84
	JS 35	128.36250	19.34133	15.43	13.26	12.23	11.35	single	2.8	1.17	2.09	2.95	3.09
	JS 353	130.09338	20.64087	14.61	12.89	12.09	11.22	single	7.0	2.71	3.73	4.35	4.37
	JS 359	130.10933	19.21942	12.90	11.83	11.09	10.46	single	5.7	1.58	2.68	4.02	4.37
	JS 382	130.19229	21.08707	16.82	14.18	12.89	12.05	single	5.3	2.35	3.23	3.58	3.58
	JS 424	130.33012	20.77756			11.38	10.70	single	8.5	2.94	4.28	5.32	5.43
	JS 430	130.35191	20.13044	16.46	13.93	12.53	11.64	single	2.9	1.54	2.47	2.98	3.01
	JS 456	130.45563	19.19642	14.50	12.75	11.65	10.83	single	2.7	1.27	2.27	3.16	3.30
	JS 466	130.49518	20.10755			11.24	10.60	single	3.1	1.13	2.13	3.34	3.62
	JS 466	130.49518	20.10755			11.24	10.60	single	5.0	1.58	2.71	3.97	4.24
	JS 473	130.55141	19.21356	13.70	12.48	11.54	10.83	single	2.6	1.01	1.75	2.87	3.19
	JS 474	130.55354	19.26777	13.50	12.15	11.22	10.48	single	2.8	1.07	1.94	3.03	3.38
	JS 478	130.56937	20.09236	14.26	12.72	11.75	10.99	single	2.9	1.36	2.31	3.21	3.40
	JS 482	130.58369	19.15161	13.51	22.51	11.39	10.70	single	6.0	2.03	3.23	4.43	4.61
	JS 494	130.66422	21.04594	15.97	13.36	12.25	11.45	poor quality	...	...	...	...	...
	JS 503	130.70198	20.57347			10.79	10.26	single	9.7	2.87	4.36	5.76	5.92
	JS 526	130.81343	20.06558	13.58	22.58	11.36	10.68	single	2.8	1.13	2.00	3.12	3.40
	JS 533	130.85422	20.56535	15.18	12.99	12.27	11.40	single	6.7	2.65	3.64	4.01	4.03
	JS 545	130.93642	21.20954	15.19	13.24	12.24	11.41	single	7.1	2.72	3.68	4.15	4.17
	JS 552	130.96190	20.36576	15.24	13.26	12.40	11.51	single	2.6	1.15	1.71	2.44	2.66
	JS 552	130.96190	20.36576	15.24	13.26	12.40	11.51	single	3.0	1.41	2.29	3.08	3.18
	JS 554	130.96590	19.91362	14.09	12.42	11.82	10.97	single	2.9	1.29	2.27	3.17	3.36
	JS 563	131.07111	18.73664	12.34	11.40	10.77	10.26	single	2.7	1.16	2.06	3.04	3.21
	JS 572	131.16982	20.19364	14.24	12.63	11.88	11.07	single	2.5	1.21	1.99	2.84	3.00
	JS 591	131.32994	19.00299			11.66	10.90	single	7.3	1.84	3.05	4.39	4.71
	JS 722	130.12083	20.88638	12.51	21.51	11.17	10.73	single	9.3	2.92	4.37	5.68	5.86
	JS 732	130.40158	21.73163	12.36	21.36	11.18	10.78	single	6.9	2.93	4.37	5.66	5.82
	JS 8	128.09782	20.99580	12.82	21.82	11.04	10.47	single	7.8	2.70	4.08	5.38	5.60
	JS 92	128.89880	18.99571	15.40	13.45	12.47	11.59	single	4.6	1.67	2.86	3.64	3.74
	JS 97	128.94492	19.87094	14.45	12.73	11.89	11.06	single	7.6	2.63	3.73	4.40	4.50
	KW 172	129.84105	19.86118	12.55	11.61	10.87	10.37	single	5.7	1.38	2.73	4.26	4.57
	KW 209	129.94614	19.82766	12.73	11.74	11.01	10.44	single	4.6	1.32	2.57	3.98	4.31
	KW 390	130.34409	18.93391	12.96	11.90	11.16	10.54	single	4.8	1.50	2.55	3.57	3.75
	KW 401	130.37794	18.87188	12.97	11.76	10.77	10.15	detected binary	3.5	1.03	1.94	2.75	2.93
	KW 415	130.41261	19.26580	13.09	12.00	11.21	10.57	single	3.0	1.09	2.00	3.32	3.72
	KW 559	129.62349	19.86250	14.03	12.60	11.67	10.93	single	5.6	1.65	2.90	3.86	4.02
	KW 560	129.73845	20.18157	13.93	12.44	11.48	10.72	single	4.7	1.78	2.99	4.03	4.20
	KW 561	129.76341	20.04378	14.44	23.44	11.87	11.05	single	5.7	1.75	3.03	4.21	4.42
	KW 564	129.81055	20.02199			12.60	11.72	single	2.8	1.41	2.29	2.93	3.02
	KW 566	129.81584	20.07058	14.99	12.92	11.74	10.87	possible binary	2.9	1.44	2.57	3.25	3.35
	KW 570	129.92097	19.99135	15.35	13.36	12.18	11.32	single	3.2	1.33	2.42	3.29	3.40
	KW 571	129.92395	20.02821	15.41	13.38	12.60	11.76	single	3.0	1.44	2.37	3.01	3.11

Table 1—Continued

Cluster	Target[1]	R.A.	Dec.	V	I	J	K	Robo-AO multiplicity	FWHM[2]	Robo-AO Contrast Distribution				
										0.5”	1”	2”	3”	
		[degrees]		[mag]					[pix]	[Δmag]				
	KW 574	130.29082	19.93535	13.64	22.64	11.50	10.76	single	2.8	1.10	1.97	3.03	3.32	
	KW 575	130.31424	20.03778	14.31	12.75	11.83	11.02	single	2.5	1.11	1.83	2.71	2.95	
	W 1010	132.14378	19.93264			12.76	11.89	single	2.8	1.57	2.40	2.90	2.98	
	W 1013	132.20824	20.44331			12.76	11.86	single	3.9	1.59	2.01	2.22	2.12	
	W 1021	132.36151	18.52210			12.24	11.39	single	5.1	1.99	3.07	3.79	3.85	
	W 302	129.40102	19.26508	13.47	22.47	11.43	10.76	single	5.7	1.82	2.98	4.11	4.35	
	W 334	129.51096	21.20547			11.88	11.15	single	6.4	2.00	3.35	4.57	4.69	
	W 352	129.56575	21.38566			12.46	11.63	single	5.9	2.33	3.54	4.20	4.28	
	W 41	128.02226	19.30014			12.61	11.79	single	7.3	2.58	3.83	4.55	4.64	
	W 560	130.08884	19.18156	13.87	12.12	11.49	10.76	detected binary	3.0	1.55	2.45	3.03	3.20	
	W 692	130.36504	19.27763	16.00	13.80	12.59	11.72	single	2.6	1.31	2.10	2.74	2.84	
	W 71	128.28523	20.44368			12.82	11.94	single	4.1	2.08	3.12	3.42	3.43	
	W 889	131.13428	21.40382			12.03	11.22	detected binary	10.4	2.25	3.35	3.87	3.93	
NGC 2264	CSIMon-0007	100.47096	9.96739			12.22	11.18	detected binary (with CSIMon-1626)	6.7	2.05	3.01	3.54	3.81	
	CSIMon-0011	100.32188	9.90900			12.83	11.55	single	8.0	2.37	3.45	4.00	4.08	
	CSIMon-0012	100.28892	9.93561			11.91	10.00	single	2.9	2.04	2.50	2.81	2.84	
	CSIMon-0017	100.38329	10.00681			13.04	12.25	single	5.3	2.27	3.38	3.90	3.94	
	CSIMon-0021	100.24771	9.99597			12.78	11.69	detected binary	5.3	2.24	3.28	3.86	4.00	
	CSIMon-0029	100.26358	9.96528			13.05	12.24	single	5.6	2.19	3.11	3.58	3.61	
	CSIMon-0033	100.28021	9.97533			12.54	11.68	single	5.2	1.98	2.93	3.56	3.62	
	CSIMon-0054	100.46288	10.02914			9.78	9.63	single	10.9	2.42	3.96	6.00	6.78	
	CSIMon-0056	100.47150	9.84650			12.96	12.00	single	5.6	2.40	3.43	3.99	4.06	
	CSIMon-0066	100.26479	10.00981			13.42	12.53	single	3.5	2.20	2.93	3.09	3.14	
	CSIMon-0087	100.27742	9.59586			12.81	12.44	single	5.9	2.24	3.49	4.35	4.42	
	CSIMon-0104	100.26742	9.86722			12.77	11.95	detected binary	15.7	1.46	2.35	2.94	3.01	
	CSIMon-0105	100.21000	9.81406			12.77	12.11	single	6.2	1.74	2.75	3.41	3.48	
	CSIMon-0108	100.31179	9.54331			12.52	11.43	single	5.1	2.36	3.26	3.63	3.62	
	CSIMon-0121	100.45421	9.68503			12.83	11.91	detected binary	6.4	2.22	3.34	3.78	3.77	
	CSIMon-0122	100.44629	9.63464			13.19	12.37	single	5.1	2.15	3.15	3.57	3.60	
	CSIMon-0135	100.25000	9.48056			13.09	12.21	single	17.4	1.39	2.60	2.97	3.01	
	CSIMon-0160	100.24921	9.86358			13.46	12.61	single	3.3	2.24	3.03	3.25	3.24	
	CSIMon-0198	100.33171	9.52900			11.93	11.11	single	8.8	2.48	3.84	4.77	4.84	
	CSIMon-0200	100.28329	9.51119			13.26	12.48	single	5.6	2.13	3.22	3.56	3.59	
	CSIMon-0223	100.23092	9.62322			12.70	11.80	single	5.2	2.25	3.43	3.88	3.93	
	CSIMon-0226	100.27229	9.55378			12.48	11.64	single	14.6	1.82	3.06	3.69	3.79	
	CSIMon-0236	100.26050	9.58217			12.36	11.65	single	6.4	2.33	3.74	4.61	4.71	
	CSIMon-0255	100.42800	9.71572			12.52	11.71	detected binary	6.6	1.94	3.20	3.74	3.82	
	CSIMon-0263	100.26079	9.58697			12.85	12.05	single	11.6	2.20	3.31	3.86	3.91	
	CSIMon-0283	100.27979	9.46333			12.21	11.36	single	21.2	1.42	3.03	5.08	5.73	
	CSIMon-0296	100.21079	9.91592			12.47	11.28	single	2.9	1.36	2.27	2.94	3.02	
	CSIMon-0298	100.27358	9.90519			12.74	11.84	single	2.9	1.54	2.25	2.65	2.68	
	CSIMon-0307	100.32458	9.56028			12.63	11.78	single	12.8	1.95	3.17	3.83	3.89	
	CSIMon-0325	100.24725	9.92228			10.65	9.70	single	7.1	1.64	2.92	4.48	4.90	
	CSIMon-0330	100.38158	9.80911			12.32	11.55	single	5.6	1.93	3.00	3.74	3.83	
	CSIMon-0341	100.22608	9.82233			13.10	11.80	single	2.9	1.65	2.24	2.61	2.63	
	CSIMon-0344	100.28958	9.59042			12.44	11.52	single	7.1	2.40	3.51	4.00	4.05	
	CSIMon-0351	100.34500	9.49411			13.72	12.94	single	2.9	1.85	2.63	2.97	2.99	
	CSIMon-0377	100.45358	9.72039			10.19	8.54	single	7.5	2.15	3.83	4.74	4.85	
	CSIMon-0379	100.27071	9.84614			12.24	11.09	detected binary	3.9	1.31	2.33	3.16	3.28	
	CSIMon-0389	100.20308	9.54517			13.28	12.40	detected binary	2.7	1.68	2.49	2.91	2.90	
	CSIMon-0394	100.28229	9.68747			12.81	11.86	possible binary	12.8	2.08	3.22	3.66	3.71	
	CSIMon-0407	100.34171	9.85353			13.54	12.70	single	2.2	1.66	2.33	2.69	2.71	
	CSIMon-0413	100.44350	9.71853			13.24	12.39	single	3.0	1.77	2.69	3.02	3.08	
	CSIMon-0427	100.17679	9.53908			13.23	12.52	single	5.2	2.01	3.08	3.55	3.57	
	CSIMon-0438	100.26421	9.50142			12.97	12.02	detected binary	2.9	1.94	2.31	2.98	3.00	
	CSIMon-0450	100.49179	9.71839			12.96	12.11	single	5.9	2.14	3.21	3.63	3.67	
	CSIMon-0461	100.47900	9.50178			13.27	12.35	single	2.9	2.19	2.91	3.18	3.21	
	CSIMon-0486	100.26679	9.81911			12.58	11.72	likely single	5.5	1.90	2.97	3.54	3.58	
	CSIMon-0498	100.19792	9.82472			11.53	10.02	detected binary	15.2	1.85	3.06	4.01	4.16	
	CSIMon-0502	100.24071	9.51403			12.95	11.82	detected binary	2.6	1.62	2.21	2.48	2.52	
	CSIMon-0515	100.40100	9.65567			13.66	12.83	single	2.9	2.12	2.83	3.09	3.09	
	CSIMon-0516	100.19729	9.81372			12.82	11.92	detected binary	3.6	1.79	2.58	2.98	3.00	
	CSIMon-0518	100.25700	9.80614			11.35	10.51	detected binary	8.4	1.83	2.78	3.15	4.02	
	CSIMon-0548	100.28558	9.71436			13.28	12.38	single	3.9	2.09	3.02	3.30	3.34	
	CSIMon-0555	100.35179	9.54589			12.94	12.05	single	3.6	2.08	2.93	3.17	3.21	
	CSIMon-0574	100.21192	9.93139			12.86	11.97	single	4.9	2.39	3.35	3.80	3.82	
	CSIMon-0578	100.45842	9.49225			12.88	12.05	single	6.4	2.15	3.24	3.82	3.86	
	CSIMon-0591	100.28229	9.47039			13.11	12.18	single	16.6	1.79	2.79	3.18	3.22	
	CSIMon-0604	100.27121	9.86239			12.74	11.98	single	14.0	1.50	2.38	2.89	2.97	
	CSIMon-0606	100.31021	9.55597			12.60	11.72	detected binary	5.4	2.29	3.49	4.05	4.08	
	CSIMon-0613	100.27408	9.80486			12.02	10.80	detected binary	4.4	1.58	2.48	3.12	3.22	
	CSIMon-0617	100.28950	9.86389			12.34	11.41	single	5.5	1.74	2.72	3.24	3.31	
	CSIMon-0618	100.20371	9.86233			9.52	8.48	likely single	10.8	1.70	3.04	5.04	5.91	
	CSIMon-0621	100.30342	9.87872			12.91	12.09	possible binary	21.1	1.10	2.03	2.61	2.66	
	CSIMon-0622	100.34079	9.75861			12.95	12.14	single	12.3	1.96	3.28	3.79	3.83	
	CSIMon-0635	100.27142	9.81544			13.58	12.75	single	3.0	1.62	2.40	2.77	2.77	

Table 1—Continued

Cluster	Target[1]	R.A.	Dec.	V	I	J	K	Robo-AO multiplicity	FWHM[2]	Robo-AO Contrast Distribution			
										0.5"	1"	2"	3"
		[degrees]				[mag]			[pix]	[Δmag]			
	CSIMon-0638	100.26904	9.91219			9.52	8.91	single	8.8	1.45	2.84	4.85	5.72
	CSIMon-0657	100.32371	9.49056			12.13	11.14	single	5.7	2.16	3.42	4.03	4.10
	CSIMon-0665	100.27471	9.45483			12.27	11.31	single	21.8	1.41	2.59	3.07	3.11
	CSIMon-0680	100.30550	9.46872			13.42	12.55	single	2.9	1.77	2.65	2.87	2.89
	CSIMon-0695	100.38542	9.63536			12.27	11.47	single	5.9	2.25	3.52	4.25	4.32
	CSIMon-0722	100.26550	9.46103			13.34	12.50	single	3.8	2.01	2.95	3.29	3.30
	CSIMon-0724	100.21950	9.73914			13.20	12.26	single	4.1	2.30	3.12	3.40	3.42
	CSIMon-0745	100.20108	9.61072			12.92	11.96	single	3.1	1.86	2.77	3.12	3.20
	CSIMon-0749	100.30892	9.44458			13.22	12.33	single	2.8	1.83	2.68	2.95	3.02
	CSIMon-0752	100.19458	9.90686			12.22	11.29	detected binary (with CSIMon-1824)	3.1	1.14	1.58	2.05	2.05
	CSIMon-0784	100.25579	9.56892			12.35	11.55	detected binary	15.1	2.12	3.25	4.00	4.09
	CSIMon-0795	100.30242	9.87533			11.49	10.21	single	4.8	1.49	2.60	3.68	3.86
	CSIMon-0804	100.23217	9.85386			12.87	12.01	single	3.1	1.58	2.46	2.90	2.94
	CSIMon-0805	100.43721	9.74456			13.18	12.38	single	2.7	1.37	2.21	2.81	2.85
	CSIMon-0810	100.29092	9.45339			11.54	10.64	single	5.5	1.58	2.83	3.90	4.05
	CSIMon-0826	100.21700	9.87050			13.10	12.21	single	19.5	1.36	2.06	2.28	1.74
	CSIMon-0890	100.22992	9.84714			13.07	12.23	possible binary	20.2	1.39	2.20	2.54	2.57
	CSIMon-0894	100.31421	9.77767			12.04	11.42	possible binary	7.1	2.20	3.79	4.89	4.96
	CSIMon-0901	100.18058	9.84986			12.57	11.73	single	4.8	1.59	2.54	3.13	3.22
	CSIMon-0932	100.18679	9.96228			12.26	11.42	single	5.4	2.44	3.59	4.42	4.51
	CSIMon-0937	100.21892	9.86831			12.69	11.72	single	15.4	0.91	1.76	2.20	2.23
	CSIMon-0948	100.36308	9.58503			12.32	11.59	single	9.2	2.56	3.94	4.87	4.91
	CSIMon-0991	100.08042	9.80833			12.81	11.89	detected binary	2.7	1.40	2.17	2.63	2.70
	CSIMon-0996	100.17217	9.85067			12.81	11.71	single	2.8	1.43	2.21	2.68	2.75
	CSIMon-1012	100.13879	9.98142			13.62	12.71	single	3.0	1.91	2.82	3.06	3.08
	CSIMon-1017	100.09892	9.92328			13.12	11.81	single	2.4	1.38	1.80	2.09	2.13
	CSIMon-1022	100.16300	9.84961			12.29	10.51	single	20.1	0.95	1.97	2.53	2.57
	CSIMon-1039	100.15600	9.92256			13.53	12.66	single	26.6	0.96	1.66	1.99	2.05
	CSIMon-1053	100.17142	9.88236			12.53	11.25	single	2.9	1.32	2.15	2.67	2.70
	CSIMon-1054	100.15221	9.84600			12.93	11.71	single	2.7	1.42	1.99	2.29	2.33
	CSIMon-1064	100.14663	9.86575			12.61	11.47	single	2.7	1.24	1.96	2.48	2.51
	CSIMon-1075	100.10608	9.80722			13.25	12.45	detected binary	7.1	2.42	3.50	3.94	3.95
	CSIMon-1085	100.13658	9.85814			12.68	11.79	single	2.7	1.25	1.95	2.39	2.45
	CSIMon-1089	100.12450	9.83622			12.22	11.56	single	4.6	1.30	2.37	3.32	3.45
	CSIMon-1099	100.17233	9.90386			11.64	10.43	single	5.4	1.48	2.71	3.96	4.14
	CSIMon-1133	99.99821	9.94008			13.14	12.31	single	4.8	1.93	2.97	3.42	3.46
	CSIMon-1149	100.12742	9.83736			12.75	11.19	detected binary (with CSIMon-1696)	28.4	0.95	1.13	1.30	1.35
	CSIMon-1174	100.05713	9.94183			12.92	11.58	single	3.0	1.84	2.65	2.95	2.97
	CSIMon-1189	100.16258	9.60000			13.30	12.40	single	2.8	1.80	2.48	2.71	2.72
	CSIMon-1199	100.17433	9.86236			12.75	10.98	detected binary	3.0	1.52	2.26	2.58	2.64
	CSIMon-1200	100.05179	9.73972			12.84	11.95	detected binary	4.9	2.15	3.21	3.58	3.59
	CSIMon-1201	100.15258	9.80639			13.04	12.21	single	4.7	2.32	3.36	3.81	3.83
	CSIMon-1217	100.15275	9.86756			12.73	11.10	single	52.8	0.31	0.85	1.21	1.27
	CSIMon-1236	100.09250	9.90792			12.29	11.31	detected binary (with CSIMon-1625)	3.1	2.00	2.45	2.91	3.00
	CSIMon-1247	100.12058	9.70478			12.91	12.02	single	6.7	2.35	3.42	3.88	3.91
	CSIMon-1248	99.94458	9.68164			12.02	11.34	detected binary	5.8	1.77	2.99	4.01	4.03
	CSIMon-1249	100.08450	9.93511			12.30	11.21	single	3.4	1.83	2.82	3.28	3.33
	CSIMon-1254	100.07079	9.77592			13.27	12.40	single	3.1	1.89	2.84	3.08	3.13
	CSIMon-1264	100.12750	9.76961			12.86	12.06	single	5.5	2.19	3.55	4.05	4.09
	CSIMon-1274	100.17258	9.80267			12.81	11.97	single	11.4	2.17	3.07	3.45	3.46
	CSIMon-1278	100.17408	9.83119			13.17	12.33	single	2.8	1.63	2.33	2.63	2.62
	CSIMon-1573	100.05242	10.09458			12.51	11.40	detected binary	3.1	1.49	2.29	2.85	2.95
	CSIMon-1625	100.09258	9.90811			12.29	11.31	detected binary (with CSIMon-1236)	3.0	1.00	1.67	2.50	2.51
	CSIMon-1626	100.47113	9.96761			12.22	11.18	detected binary (with CSIMon-0007)	4.8	2.08	3.08	3.60	3.90
	CSIMon-1696	100.12750	9.83758			12.75	11.19	detected binary (with CSIMon-1149)	13.7	0.82	0.75	1.43	1.47
	CSIMon-1824	100.19458	9.90686			12.22	11.29	detected binary (with CSIMon-0752)	3.1	1.67	2.26	2.79	2.99
	CSIMon-6975	99.97171	10.02050			13.48	12.15	detected binary	2.4	1.45	1.73	1.94	1.91

[1]In the Pleiades, the naming convention follows that in Stauffer et al (2007) for the stars from that list. For other stars from Bouy et al (2015), we generally chose to use the name from the first published survey that included the star as a likely Pleiades member. Names are SIMBAD-compliant if preceded by "Cl* Melotte 22" with the exception of those noted as "s" which come from the catalog of Sarro et al. (2014) - http://vizier.cfa.harvard.edu/viz-bin/VizieR?-source=J/A+A/563/A45. In Praesepe, we attempted to follow the standard convention of referring to the star by the name given to it in the first paper which ascribed cluster membership. Names are SIMBAD-compliant if preceded by "Cl* NGC 2632" with the exception of those noted as "AD", a nomenclature originating in Kraus & Hillenbrand (2007) to refer to stars first identified as Praesepe members by Adams et al. (2002). In NGC 2264, the naming convention is that of the Stauffer et al. Spitzer variability survey (https://irsa.ipac.caltech.edu/data/SPITZER/CSI2264/). Names are SIMBAD-compliant as recorded.

[2]The Robo-AO platescale is sampled at 21.55 milli-arcsec/pixel

Table 2. Basic Characteristics of Detected Binaries

Cluster	Binary	Significance σ	Projected Separation [arcseconds]	Position Angle [degrees]	Optical Brightness Ratio [Δmag]	Mass Ratio [$q = m_2/m_1$]
Pleiades	AK IV-314	9.7	1.03	121.2	2.37±0.05	0.53
	DH 056	10.6	2.52	244.1	2.78±0.10	0.33
	DH 193	9.7	0.90	83.9	1.86±0.08	0.54
	DH 446	9.4	2.28	64.2	3.39±0.17	<0.23
	DH 800	19.3	2.25	95.6	2.41±0.05	0.52
	DH 896	11.7	0.96	5.8	1.38±0.05	0.57
	HCG 86	11.1	1.21	185.2	0.75±0.04	0.71
	HCG 123	8.4	0.78	253.6	1.67±0.06	0.50
	HCG 354	6.0	0.45	179.9	1.21±0.07	0.63
	HCG 502	9.3	0.67	50.4	0.52±0.06	0.82
	HII 1114	4.1	0.44	130.8	2.58±0.11	0.40
	HII 1306	7.9	0.60	60.6	0.58±0.04	0.87
	HII 134	19.1	1.84	269.4	0.27±0.05	0.93
	HII 2193	6.0	0.66	277.8	2.45±0.16	0.38
	HII 2368	9.7	0.65	85.4	2.55±0.15	0.39
	HII 2602	6.1	0.59	131.4	0.92±0.06	0.71
	HII 357	12.8	0.47	64.5	2.57±0.11	0.44
	HII 659	15.7	3.42	233.2	3.15±0.09	0.40
	HII 890	12.3	1.19	227.7	4.62±0.16	<0.18
	HII 906	12.3	1.44	35.4	2.01±0.07	0.46
	PELS 115	30.5	3.34	271.1	3.17±0.07	0.36
	s4236066	10.5	0.62	159.2	2.01±0.07	0.41
	s4337464	13.3	1.91	260.1	0.27±0.05	0.92
	s4713435	5.1	1.63	291.5	4.54±0.22	<0.17
	s4955064	7.1	0.64	4.1	0.74±0.05	0.71
	s5035799	23.3	4.59	252.4	3.60±0.08	0.20
	s5197248	15.2	3.11	16.5	2.62±0.06	0.34
	s5216838	14.5	0.92	68.7	2.66±0.06	0.41
	s5305712	3.5	0.23	70.5	1.47±0.03	0.50
	SK 432	4.7	0.34	112.5	1.19±0.13	0.57
	SK 638	10.6	0.33	151.9	1.27±0.16	0.56
	SK 671	7.6	1.62	330.6	2.16±0.11	0.44
Praesepe	AD 3085	12.7	1.22	86.8	0.48±0.06	0.83
	AD 3349	11.9	2.54	347.3	3.37±0.11	0.32
	JC 10	10.5	1.38	266.5	4.55±0.09	0.24
	JS 160	9.4	0.67	128.8	2.69±0.12	0.39
	JS 19	6.2	0.33	295.9	0.98±0.09	0.67
	KW 401	5.5	1.77	237.6	3.21±0.20	0.43
	W 560	10.1	2.50	192.8	0.55±0.76	0.86
	W 889	15.5	2.04	63.8	2.39±0.06	0.42
NGC 2264	CSIMon-0007	15.2	1.05	34.5	1.28±0.06	···
	CSIMon-0021	10.3	1.19	326.6	2.60±0.06	···
	CSIMon-0104	11.3	3.47	356.1	3.50±0.15	···
	CSIMon-0121	16.9	4.02	91.6	2.12±0.08	···
	CSIMon-0255	10.4	2.31	199.0	2.83±0.09	···
	CSIMon-0379	7.4	0.80	56.7	2.84±0.15	···
	CSIMon-0389	11.8	2.28	318.6	2.87±0.16	···
	CSIMon-0394	5.5	0.86	266.2	4.10±0.23	···
	CSIMon-0438	9.4	1.21	140.9	2.03±0.11	···
	CSIMon-0498	12.9	2.93	175.9	3.02±0.07	···
	CSIMon-0502	6.1	0.94	149.4	2.40±0.12	···
	CSIMon-0516	21.6	6.14	255.8	0.94±0.07	···
	CSIMon-0518	8.5	1.31	146.8	0.56±0.04	···
	CSIMon-0606	18.5	3.26	266.5	3.40±0.10	···
	CSIMon-0613	9.0	0.33	119.1	1.65±0.12	···
	CSIMon-0784	8.5	0.79	232.8	3.48±0.10	···
	CSIMon-0991	8.8	3.19	350.0	2.51±0.16	···
	CSIMon-1075	17.6	5.30	0.4	0.96±0.05	···
	CSIMon-1149	4.5	0.91	18.2	0.48±0.14	···
	CSIMon-1199	9.6	2.09	352.7	0.61±0.05	···
	CSIMon-1200	8.1	0.51	267.3	2.50±0.11	···
	CSIMon-1236	5.0	0.73	16.9	0.71±0.06	···
	CSIMon-1248	14.2	2.41	173.5	3.22±0.08	···
	CSIMon-1573	5.1	0.82	175.0	4.05±0.13	···
	CSIMon-1824	4.5	0.89	205.1	0.96±0.05	···
	CSIMon-6975	10.3	2.37	51.3	1.08±0.12	···